# Traceable charge measurement of the pulses of a 27 MeV electron beam from a linear accelerator

Published by IOP Publishing for Sissa Medialab

Received: *September 29, 2016*
Revised: *January 13, 2017*
Accepted: *February 6, 2017*
Published: *March 3, 2017*

2017 JINST 12 P03003

# Traceable charge measurement of the pulses of a 27 MeV electron beam from a linear accelerator

**A. Schüller,**[1] **J. Illemann, F. Renner, C. Makowski and R.-P. Kapsch**

*Physikalisch-Technische Bundesanstalt,*
*Bundesallee 100, 38116 Braunschweig, Germany*

*E-mail:* andreas.schueller@ptb.de

Abstract: This work presents a detailed description of measuring devices and calibration procedures which enable the nondestructive (non-intercepting) absolute measurement of the charge of individual beam pulses (macro-pulses) from an electron linear accelerator traceable to primary standards with high accuracy, i.e. with an expanded measurement uncertainty < 0.1 %. In particular, we demonstrate the readout and calibration of a Bergoz integrating current transformer which is frequently applied at many different types of accelerators as a beam intensity monitor. The current transformer signal is calibrated against the absolute charge measurement by means of a custom-made compact Faraday cup with a high degree of collection efficiency for electron beams in the energy range of 6 MeV to 50 MeV (99.2 % at 27 MeV), which is well known from measurements and consistently described by Monte Carlo calculations.

Keywords: Beam-line instrumentation (beam position and profile monitors; beam-intensity monitors; bunch length monitors); Instrumentation for particle accelerators and storage rings - high energy (linear accelerators, synchrotrons)

[1]Corresponding author.



doi:10.1088/1748-0221/12/03/P03003

## Contents



2017 JINST 12 P03003

## 1 Introduction

The National Metrology Institute of Germany, the Physikalisch-Technische Bundesanstalt (PTB), operates a custom-designed electron linear accelerator (linac) for fundamental research in dosimetry for radiation therapy [1]. A drawing of the facility is shown in figure 1. The accelerator operates on the same principle as medical linacs applied in cancer treatment in hospitals. Here, for the generation of high-energy photon radiation a pulsed electron beam with energies of several MeV is shot at a metal target for the generation of bremsstrahlung with therapeutically relevant dose rates. In contrast to factory-made medical linacs, all electron beam parameters of PTB's research linac are continuously adjustable and can be measured with a high degree of accuracy. In this way, it is possible to study radiation effects as a function of their fundamental physical quantities such as energy, current and fluence.

One crucial quantity is the charge per beam pulse (macro-pulse[1]) which is directly proportional to the dose per pulse of the generated photon radiation. Due to the discontinuous operating principle of a conventional electron linac (the acceleration of electron bunches in cavities by a short (some

[1] A beam from a conventional linac consists of macro-pulses which are composed of fine structure micro-pulses from the train of electron bunches created by the accelerating microwave (about 3 GHz in our case).

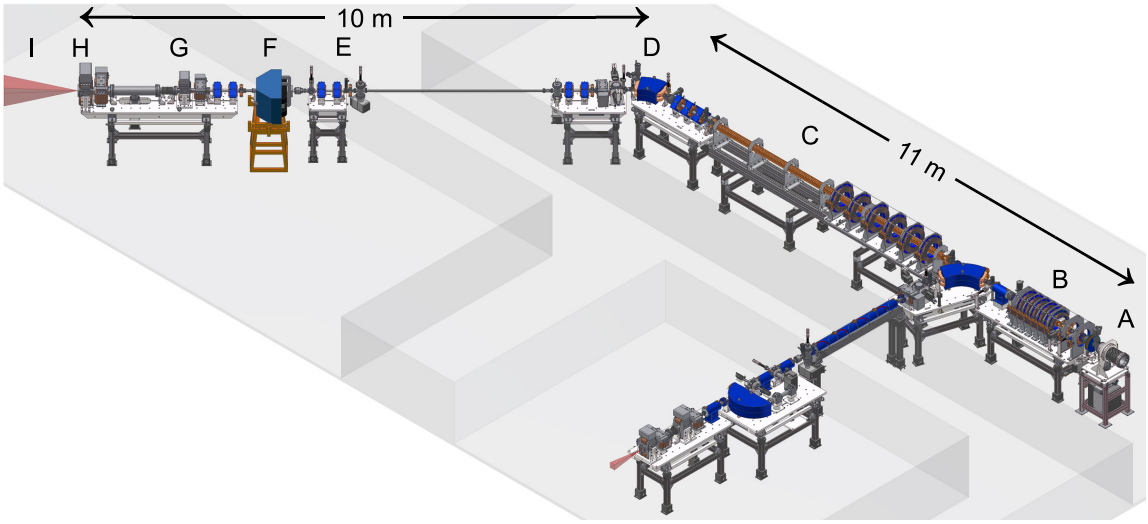


**Figure 1**. Drawing of PTB's custom-designed electron linac for fundamental research in dosimetry for radiation therapy. A: electron gun. B: low-energy section (0.5 MeV to 10 MeV). C: high-energy section (6 MeV to 50 MeV). D: dipole magnet for energy separation and beam dump. E: collimator. F: magnetic spectrometer. G: beam intensity monitor (current transformer). H: Faraday cup or metal target for bremsstrahlung generation. I: photon radiation. Gray areas: walls of the radiation protection bunker. Length of acceleration path A–D: about 11 m. Length of high-energy beamline D–H: about 10 m.

$\mu$s) high power (several MW) microwave pulse) the charge of the electron pulses differs somewhat from pulse to pulse. The charge of an optimized beam from PTB's research linac typically fluctuates by about 3 %.

This work presents a detailed description of measuring devices and calibration procedures in order to enable the nondestructive (non-intercepting) absolute measurement of the charge of individual beam pulses from the linac traceable to primary standards. In particular, we demonstrate the readout and calibration of an Integrating Current Transformer (ICT) [2, 3], commercially available from Bergoz Instrumentation [4], which is frequently applied as a beam intensity monitor or even for the absolute charge measurement at many different types of accelerators. The signal from this beam intensity monitoring system is calibrated against the absolute charge measurement by means of a temporarily installed Faraday cup which is capable of collecting almost all electrons of the high-energy beam. Its collection efficiency is known with great accuracy from experiment and simulation, as described below.

The beam charge measurement was one necessary condition for the realization of a benchmark experiment for the verification of the absolute accuracy of Monte Carlo (MC) simulations of the absorbed doses for high-energy radiotherapy [5, 6]. In principle, MC-calculated doses are doses per incident particle of the radiation source. Usually in experiments, the number of source particles is inaccessible and, therefore, MC-calculated doses have to be adequately normalized to benchmark them against equally normalized experimental doses. In the benchmark experiment, the number of source electrons is known via the beam charge and, consequently, no dose normalization is necessary, i.e. doses are comparable in an absolute manner.

The electron beam energy in the benchmark experiment mentioned above was chosen to be about 27 MeV [7], since the resultant photon radiation covers the maximum energy range used in



2017 JINST 12 P03003

clinical radiation therapy [5]. And the used pulse charges were in the range of −60 nC in order to generate the needed radiation dose. For this reason, the focus of this work is on that energy and charge range. The aim for the overall relative uncertainty of the benchmark experiment was $u < 1$ % ($k = 2$).[2] Thus the uncertainty contribution from the pulse charge measurement should be in the range of 0.1 % ($k = 2$).

In many experiments ICTs are used as absolute instrument for the charge measurement without any uncertainty analysis. In some experiments the ICT is cross calibrated against a Faraday cup [9–13]. Deviations of several percent are regarded as good agreement [12–14]. However, to achieve absolute accuracy of about 0.1% requires a careful experimental setup and sophisticated calibration procedures.

To achieve this goal three problems must be solved: first, the accurate measurement of charge pulses traceable to a primary standard as described in section 3; second, the acquisition of the beam intensity monitor signal without significant noise contributions and its calibration against the simultaneously measured charge pulses from the Faraday cup as described in section 4; and third, the determination of a correction factor due to charge losses of the Faraday cup, i.e. the determination of its collection efficiency, as described in section 5.

## 2 Setup

The beam intensity monitoring system described in this work is installed at the beamline from the high-energy section (6 MeV to 50 MeV) of PTB's research linac ("D"–"H" in figure 1). The experimental data presented below are collected at a beam energy of about 27 MeV, while the variable pulse repetition rate (1 Hz to 100 Hz) was set at 5 Hz. This corresponds to the setting in the benchmark experiment mentioned above [5, 6]. The duration of a beam pulse from the linac (macro-pulse length) amounts to a maximum of 2.5 $\mu$s. The charge per pulse of the optimized beam amounts to about −60 nC. The pulse charge can be varied without influencing the position of the beam in the beamline by the variation of the width (0.5 mm to 3 mm) of the slit diaphragm for reducing the kinetic energy spread behind the dipole magnet for energy separation at the end of the high-energy section ("D" in figure 1). In order to confine the beam divergence and to reduce the "beam halo" [15], a removable collimator with an opening of about 10 mm in diameter is placed on the axis at the start of the beamline ("E" in figure 1). For the analysis of the beam profile and the beam divergence, several wire scanners (BPM80, National Electrostatics Corp.) and removable YAG:Ce screens are installed at the beamline. For the accurate determination of the kinetic energy of the electrons a magnetic spectrometer ("F" in figure 1) is used which is described elsewhere [7].

For the nondestructive measurement of the charge of the electron pulses a Bergoz ICT (in-flange version, turns ratio 50:1, ICT-CF4.5/34.9-070-50:1-UHV, SN 1650) [2–4] is mounted directly as a vacuum component in the beamline ("G" in figure 1). A photo of the ICT is shown in figure 2a. A bare wire called "Q-loop" [16, 17] is mounted in situ by means of two additional flanges with an electrical feedthrough on both sides of the ICT as shown in figure 2b. The Q-loop can carry charge pulses from a pulse generator to simulate the pulsed electron beam for test purposes.[3]

[2]The expanded uncertainties [8] quoted in this article are based on a standard uncertainty multiplied by a coverage factor $k = 2$ (two standard deviations), providing a coverage probability of approximately 95 %.

[3]ICT models with a preinstalled calibration winding are available from the manufacturer [4].



2017 JINST 12 P03003

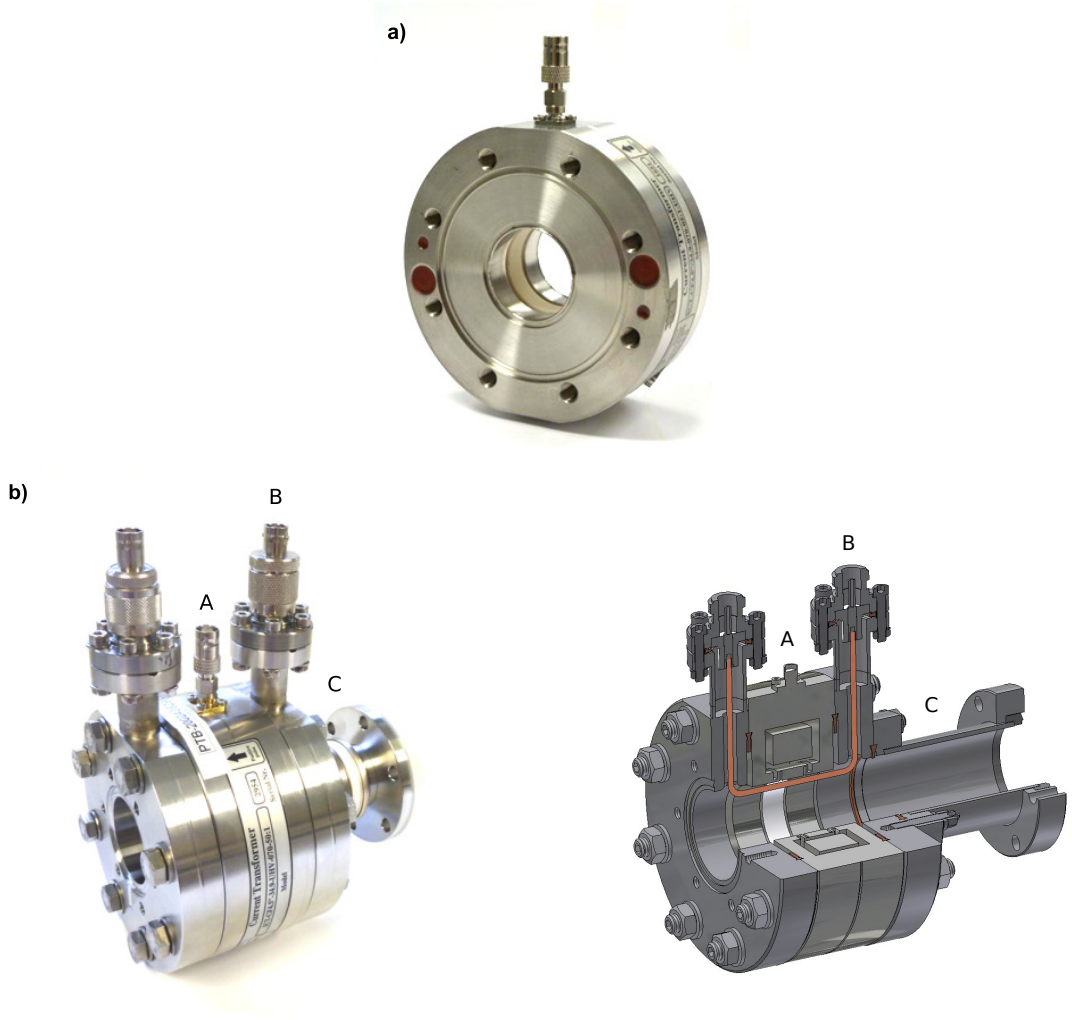


**Figure 2**. a) Photo of the Bergoz ICT. b) Photo (left) and sectional drawing (right) of the ICT (A) with an in situ wire through the ICT (Q-loop) screwed on electrical feedthroughs at additional flanges (B) and a vacuum ceramic break (C).

The ICT is a passive alternating current transformer which works on the principle of the Rogowski coil [18]. The pulsed electron beam crosses through a highly permeable ring core acting as a single turn primary winding of the transformer that drives magnetic flux in the core to induce a current in a secondary winding on the same core [15, 19, 20]. The secondary current produces the transformer output voltage at a 50 Ω resistor. Since a transformer cannot transmit a direct current component, the secondary current and thus the output voltage feature a signal droop [15, 19–21]. In order to obtain a signal which represents the beam intensity with good absolute accuracy without effects due to variations of the pulse shape, a significant signal droop during the period of the beam pulse has to be prevented. The droop time constant scales with the square of the number of turns of the secondary winding [15, 19, 20]. Therefore an ICT model with the maximum available number of turns (turns ratio 50:1) is used, where the signal droop during the maximum 2.5 $\mu$s duration of the beam pulse is small (nominal $< 2$ %/$\mu$s).



2017 JINST 12 P03003

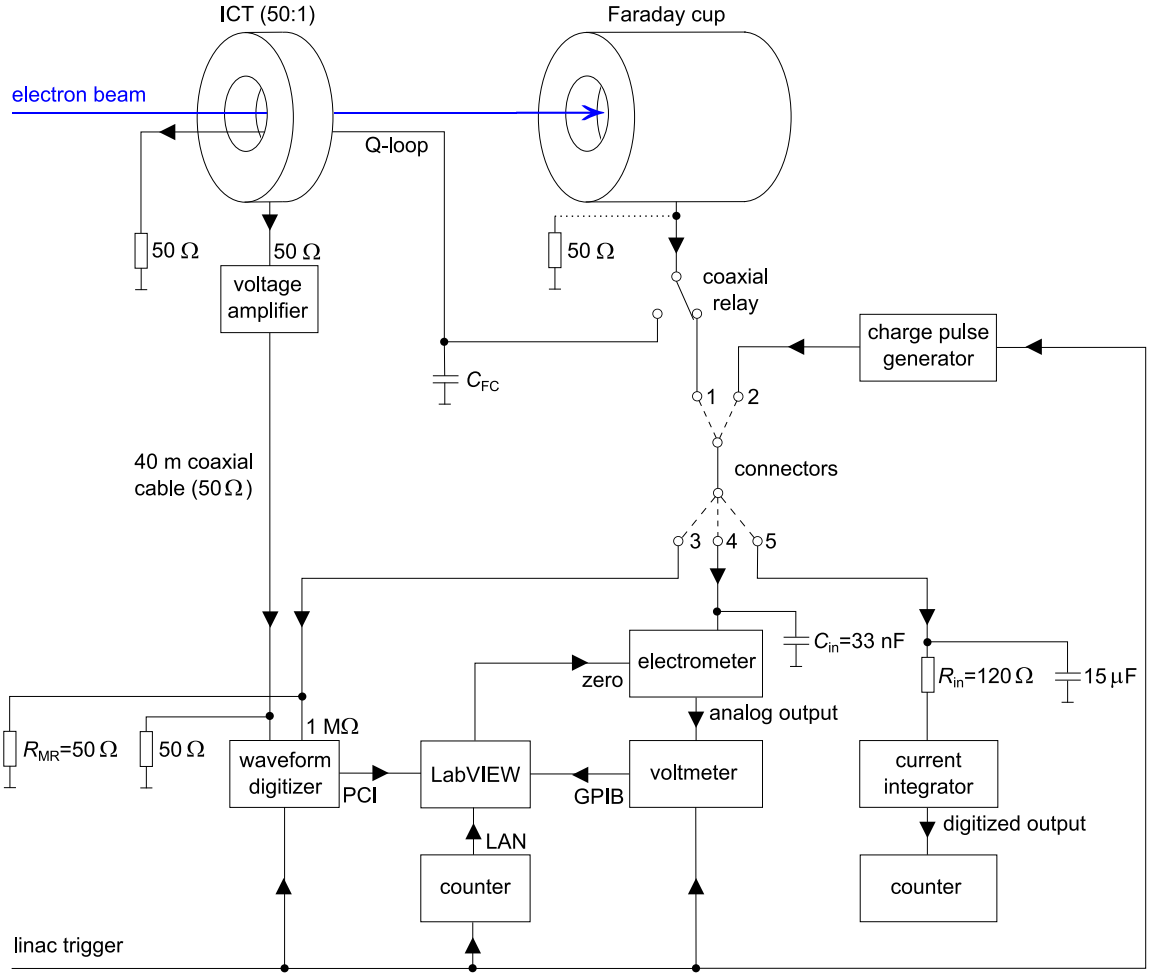


**Figure 3**. Block diagram of the wiring and signaling of the setup. Either connector 1 (from the Faraday cup) or 2 (from the charge pulse generator) is plugged into either connector 3 (to the waveform digitizer), 4 (to the electrometer), or 5 (to the current integrator). The terminating resistor at the Faraday cup (at the dotted wire) is not connected during a charge measurement. Waveform digitizer: Spectrum M3i.4142. Electrometer: Keithley 616. Current integrator: Ortec 439. Voltmeter: Agilent 3458A. Charge pulse generator: CGC QCAL-1. Voltage amplifier: FEMTO HVA-200M-40-B.

The voltage-time integral of the ICT output pulse is proportional to the charge of the inducing beam pulse. The ICT output voltage is recorded by means of a fast (sampling rate 250 MS/s) waveform digitizer (also referred to as a transient recorder or PC oscilloscope) with 14-bit resolution (Spectrum M3i.4142). Due to the high radiation exposure in the vicinity of the beamline, active electronic devices like the waveform digitizer are placed outside the radiation protection bunker. In order to improve the signal-to-noise ratio at the end of the required long transmission line (about 40 m, type Belden H155A01) between the ICT and the waveform digitizer, a wide band (200 MHz) low noise voltage amplifier (FEMTO HVA-200M-40-B with 50 Ω input, DC coupled) is used as a preamplifier at the output of the ICT. The maximum output voltage of the preamplifier with linear amplification is ±1 V. Since the used ICT with turns ratio 50:1 induces at the maximum beam pulse amplitude of −100 mA a maximum of −0.05 V at the 50 Ω input impedance of the preamplifier,



2017 JINST 12 P03003

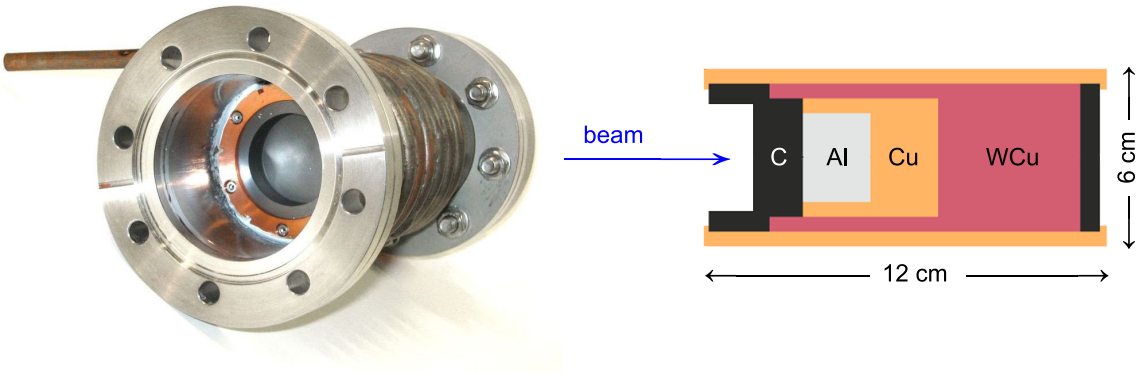


**Figure 4**. Left: photo of the Faraday cup glued into a tubular vacuum adapter (DN 63 CF) with a water cooling coil welded on the outside wall. Right: drawing of the structure of the Faraday cup. C: 1.5 cm, Al: 2 cm, Cu: 2 cm, WCu: 4.2 cm. The WCu-alloy contains 80 % tungsten.

the amplification factor is set to 10 (20 dB) and the input range of the waveform digitizer is set to ±0.5 V. The wiring is shown in the block diagram in figure 3. The preamplifier is enclosed by a pile of lead bricks for radiation protection of its electronic components.

The beam intensity monitoring system is calibrated against an in-vacuum Faraday cup shown in the photo on the left in figure 4. The Faraday cup is installed in the beamline behind the current transformer (at "H" in figure 1). Since the measurement with a Faraday cup is inherently destructive, the device is installed temporarily and then replaced by the metal target for the generation of the desired photon radiation after the calibration is completed.

The design of the custom-made Faraday cup is optimized by means of simulations with the MC code EGSnrc [22, 23] with regard to high collection efficiency for electron beams with energies of 10 MeV to 50 MeV at small overall size of the Faraday cup. By the utilization of MC methods it is possible to reduce the size in comparison to the large Faraday cups in early experiments with electron beams of similar energies [16, 24–26] without a reduction in the collection efficiency. In contrast to these previous experiments, the Faraday cup in our setup shares the same vacuum as the beam. This avoids disturbing effects due to scattering at vacuum foils of beam exit or entry windows [16, 27]. The Faraday cup is 12 cm long, 6 cm in diameter with an open aperture 3.6 cm in diameter. It is composed of a sequence of 1.5 cm carbon (C), 2 cm aluminum (Al), 2 cm copper (Cu), and 4.2 cm copper-tungsten alloy (WCu, 80 % tungsten). The right side of figure 4 shows a drawing of the structure of the Faraday cup. The entrance is made of graphite (carbon) in order to minimize the fraction of (low energy) backscattered electrons. During the experiments, the vacuum is kept at $< 10^{-8}$ mbar by means of a turbomolecular pump between the ICT and the Faraday cup in order to avoid neutralization of the collected charges by positive ions from residual gas molecules ionized by the beam.

The measurement of the charge of the electron pulses collected by the Faraday cup is carried out by an electrometer (connectors 1 to 4 in figure 3), by means of a high precision resistor at the second input of the waveform digitizer (connectors 1 to 3 in figure 3), or a current integrator (connectors 1 to 5 in figure 3) as described in section 3 in detail. If the Faraday cup is not connected



2017 JINST 12 P03003

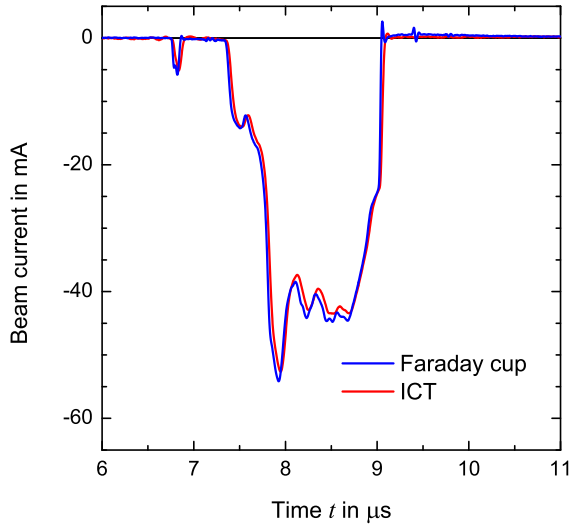


**Figure 5**. Current from a typical beam pulse as a function of time with respect to the linac trigger as recorded simultaneously by means of the two independent channels of the waveform digitizer from the Faraday cup (blue curve) and from the current transformer (red curve). Faraday cup output is terminated with 50 Ω (dotted wire in figure 3).

to a measuring device it needs to be terminated by a resistor in order to avoid potentially dangerous high voltages.

Figure 5 shows the current from a typical beam pulse as a function of time as recorded simultaneously by means of the two independent channels of the waveform digitizer from the Faraday cup and from the ICT. The beam pulse is time delayed with respect to the linac trigger ($t = 0$) by at least 6.5 $\mu$s. Neither the ICT nor the Faraday cup can resolve the micro-pulses (< 0.08 ns length) which form a beam pulse. Since the fine structure is similarly smoothed out for both devices, the observed shape of the beam pulse is similar.[4]

The conditioning of the signal from the ICT and its calibration against the Faraday cup is described in detail in section 4. For the experimental determination of the collection efficiency of the Faraday cup by a cancellation measurement [16], the electrons collected by the Faraday cup can be returned through the ICT via the "Q-loop" wire [16, 17] (see figure 3). The determination of the collection efficiency is described in detail in section 5.

## 3 Traceable measurement of charge pulses

The acquisition of the charge collected by the Faraday cup is realized by three independent methods and, thereby, traced back to different measurands and primary standards: first, the charge measurement by a Keithley 616 electrometer (connector 4 in figure 3) which is calibrated by a reference charge; second, the determination of the mean pulse charge of many pulses by the measurement of the mean current by means of an Ortec 439 current integrator (connector 5 in figure 3) which

[4]The optimization of the ICT for a low signal droop increases its rise time (20 ns). The response of the Faraday cup is determined by the time constant (18 ns) of the RC element formed by the capacity of the Faraday cup (0.36 nF) and its termination (50 Ω).



2017 JINST 12 P03003

is calibrated by a reference current; and third, the measurement of the time-resolved voltage drop across a high precision measuring resistor by means of the M3i.4142 waveform digitizer (connector 3 in figure 3) which is calibrated by a reference voltage.

The accuracy of each of the three acquisition methods may be questioned due to insufficient knowledge of possible perturbing errors. For example an electrometer, actually built to read the charge of low quasi-continuous currents, may be saturated at short pulses of relatively high currents. The determination of the mean pulse charge from the current measurement by means of the current integrator may be erroneous due to the integration of a continual offset or leakage current between the short pulses. The reading of the waveform digitizer may be inadequate owing to attenuation, transit time and bandpass effects on the pulse shape due to the long coaxial cable and due to signal reflections. But if the results of the three methods are consistent, then significant errors are implausible.

A single charge pulse cannot be measured simultaneously by two of the utilized devices. Therefore for the comparison of the measurement methods a custom-made charge pulse generator ("QCAL-1", CGC Instruments [28], Chemnitz, Germany) based on a radio frequency vacuum tube pentode (Telefunken PL 504) output is used as a constant source of charge pulses instead of the fluctuating pulse charges from the linac caught by the Faraday cup (connector 2 instead of 1 in figure 3). The current amplitude and the pulse length of the charge pulses from this device approximately match the dimensions of the linac beam pulses.

The following subsections describe the charge acquisition procedures.

### 3.1 Electrometer

The measurement of the charge of a pulse by an electrometer has the advantages that the shape of the pulse, impedance mismatches, signal reflections, and the cable attenuation are irrelevant. The used Keithley 616 electrometer has an analog circuit without any digital filters or postprocessing. In the used charge measurement mode, effects due to room temperature fluctuations are negligible. The calibration coefficient is known as having long-term stability through experience with this device over decades. A Keithley 616 electrometer is utilized as well by Vognar et al. [26] for the precise measurement of the Faraday cup current of a 5 MeV to 25 MeV electron beam.

For the traceable calibration of the used "$10^{-8}$ C" charge range ("fast" mode) a reference charge $Q_{\mathrm{ref}}$ is generated by means of custom-made air capacitors[5] with stable[6] and traceably calibrated[7] capacitance $C_{\mathrm{air}}$ and a reference voltage $U_{\mathrm{ref}}$ from a calibrated voltage source (HP3245A).[8] The capacitor is connected in series with the electrometer and charged by a reference voltage of $-10\ \mathrm{V} < U_{\mathrm{ref}} < -100\ \mathrm{V}$. Different capacitors with $C_{\mathrm{air}}$ between 100 pF and 10 nF are used in order to cover

[5]Since the capacitors have air as their dielectric medium, the capacity shows no detectable frequency dependence. So their capacity from accurate calibration with AC voltages (6 different frequencies between 50 Hz and 10 kHz) can be used at DC voltage.

[6]The capacitance is known as having long-term stability (maximum drift ±0.005 % per year) through repeated calibrations over three decades. The dependence on temperature is small (0.0017 %/K). The dependence on air pressure is negligible (0.000054 %/mbar).

[7]The capacitors are calibrated annually traceable to PTB primary standards (expanded uncertainty $u(C_{\mathrm{air}})/C_{\mathrm{air}} = 0.0007$ %).

[8]The output voltage of the HP3245A voltage source is verified (maximum deviation 0.0005 %) by means of an Agilent 3458A multimeter calibrated traceable to PTB primary standards.



2017 JINST 12 P03003

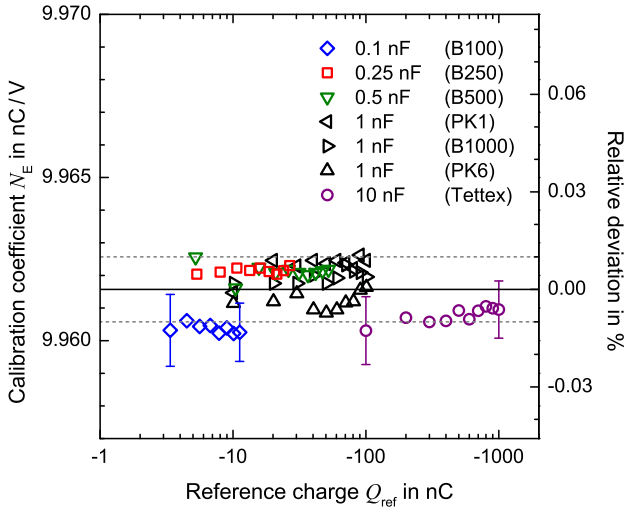


**Figure 6**. Calibration coefficient $N_E$ of the used Keithley 616 electrometer in the "$10^{-8}$ C" charge range as a function of the reference charge $Q_{ref}$ generated by a reference voltage between −10 V and −100 V and seven different capacitors with nominal capacities $C_{air}$ and type as indicated. For reasons of clarity, error bars are shown only for lowest and largest value from lowest and largest capacitor, respectively. Dashed lines: limits for 0.01 % deviation from mean value.

a large charge range and at the same time to survey the scattering of the results for the estimation of the uncertainty. A 10 MΩ resistor limits the maximum current to some $\mu$A and prolongs the charging to some 100 ms which avoids the saturation of the electrometer by a short high current pulse during a change in the reference voltage $U_{ref}$. The reference charge $Q_{ref}$ collected by the electrometer at a change in the reference voltage by $\Delta U_{ref}$ amounts to $Q_{ref} = C_{air} \cdot \Delta U_{ref}$. The electrometer responds with a change in its analog output voltage of $\Delta U_{out}$ which is measured by a calibrated 8.5-digit multimeter of type Agilent 3458A.[9]

The calibration coefficient is

$$\begin{aligned} N_E &= Q_{ref}/\Delta U_{out} \\ &= C_{air} \cdot \Delta U_{ref}/\Delta U_{out} \,. \end{aligned} \tag{3.1}$$

The expanded uncertainty of the reference charge is estimated to be $u(Q_{ref})/Q_{ref} = 0.0085$ % taking into account effects due to laboratory temperature and long-term drift on $C_{air}$. The expanded uncertainty of the measurement of the change in the analog output voltage of the electrometer is estimated to be $u(\Delta U_{out})/\Delta U_{out} = 0.0035$ %. The resulting combined expanded uncertainty of a determined calibration coefficient is $u(N_E)/N_E = 0.01$ %. Figure 6 shows the calibration coefficients as a function of the reference charge determined using seven different capacitors. Almost all results agree within the estimated ±0.01 % (gray dashed lines). The calibration coefficient is independent of the charge, i.e. the electrometer shows no non-linearities, in the entire range (−1 nC to −1 $\mu$C). The deviation from the nominal value of 10 nC/V amounts to about −0.4 % for the Keithley 616 used here (SN 46534A). Statistical evaluation of the mean value of the seven measurements with

[9]The used ±100 V measuring range is verified by means of a Knick DC-Calibrator JS3010 traceably calibrated to PTB primary standards (deviation 0.001 %, offset < 0.1 mV, agreement within uncertainty).



2017 JINST 12 P03003

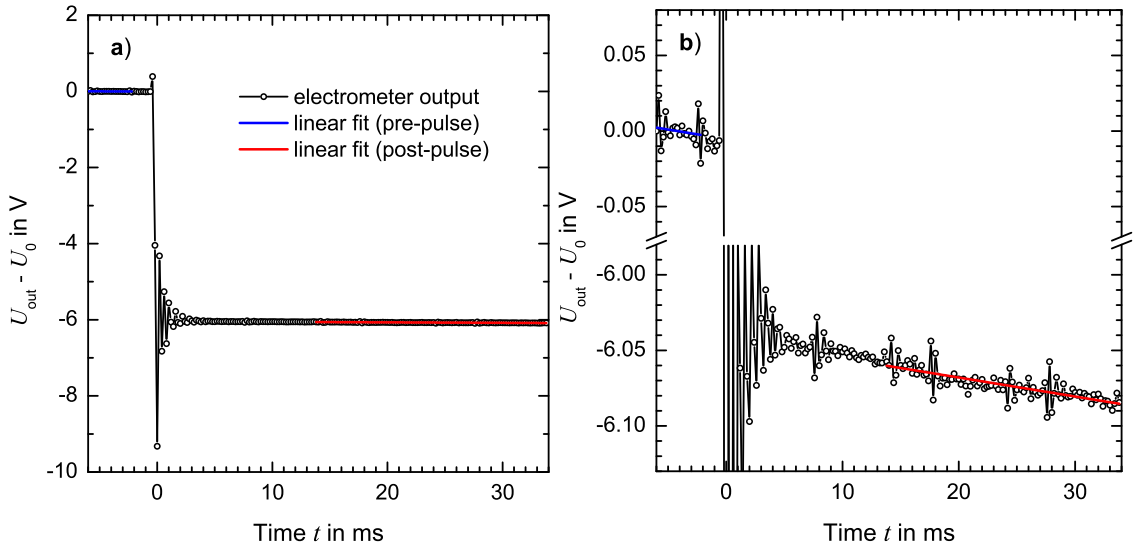


**Figure 7**. a) electrometer output voltage difference $U_{\text{out}} - U_0$ as a function of the time span $t$ with respect to the charge pulse from the pulse generator (with $C_{\text{in}} = 33$ nF at the electrometer input). $U_0$ is the electrometer output voltage before the pulse at $t = -6$ ms. Red line: best linear fit to post-pulse data from $t = 14$ ms to 34 ms. Blue line: linear fit to pre-pulse data from $t = -6$ ms to $-2$ ms, where the slope is fixed to be the same as for the post-pulse data. b) same data with detail enlargement (y-axis break). Pre-pulse and post-pulse linear fit have the side condition that both have the same slope.

different capacitors results in an expanded measurement uncertainty of the calibration coefficient of the electrometer for quasi-static charge measurement of $u_{\text{cal}}(N_{\text{E}})/N_{\text{E}} = 0.0071$ %.

Every charge pulse from the Faraday cup with a linac beam or from the QCAL-1 charge pulse generator fed into the electrometer input (connectors 1 to 4 or 2 to 4 in figure 3) causes a voltage step at its analog output. The output voltage $U_{\text{out}}$ is measured by a high-accuracy digital multimeter (Agilent 3458A) in the ±100 V measuring range ("voltmeter" in figure 3).[10] The 3458A is controlled via its GPIB interface by a LabVIEW program. Whenever its external trigger input receives a signal (6 ms before the charge pulse), the device records 200 data points with an interval of 200 $\mu$s. For each pulse the resulting dataset is sent separately to the PC in real time.[11] If $U_{\text{out}}$ exceeds −100 V, then the electrometer is discharged by closing the remote "Zero Check" contact[12] ("zero" in figure 3) and by subsequently connecting a 1 kΩ resistor at the input by means of relays for a sufficiently fast discharge in order to miss as few linac pulses as possible during this process. For overload protection in case of a computer breakdown, a stand-alone device (not shown) with analog circuits monitors the output voltage and closes the "Zero Check" relay immediately, as soon as the voltage reaches −120 V (limit of the 3485A in the ±100 V range).

Figure 7a shows the electrometer output voltage difference $U_{\text{out}}(t) - U_0$ as a function of the time span $t$ with respect to the charge pulse from the QCAL-1 charge pulse generator. $U_0$ is the

[10] $U_{\text{out}}$ between connectors "X1" and "Guard".

[11] The used memory format of the 3458A is "DINT" in order to ensure a sufficient transfer rate. Since the subsequent communication requires time too, the pulse repetition rate is limited to $f_{\text{P}} \leq 10$ Hz.

[12] pin J113 D



2017 JINST 12 P03003

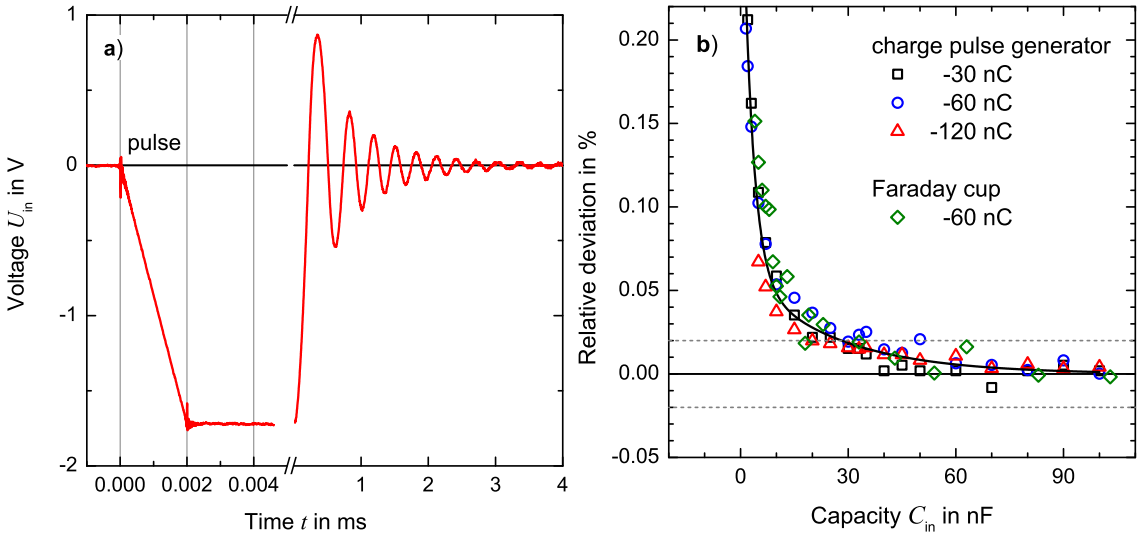


**Figure 8**. a) voltage $U_{\text{in}}$ at the electrometer input as a function of time for a charge pulse of nominal −60 nC with 2 $\mu$s length while a capacitor of $C_{\text{in}}$ = 33 nF is installed at the input. Note the different time scale before and after the x-axis break. b) relative deviation of the mean electrometer signal $\langle S_{\text{E}} \rangle$ from its asymptotic value at large $C_{\text{in}}$ as a function of $C_{\text{in}}$ for pulses from the charge pulse generator of nominal −30 nC (squares), −60 nC (circles), and −120 nC (triangles) with 2 $\mu$s length. Diamonds: relative deviation of the electrometer signal for pulses of about −60 nC from the Faraday cup with a linac beam, normalized to the beam pulse charge simultaneously measured by means of the current transformer. Curve: to guide the eye. Dashed lines: limits of ±0.02 % deviation.

initial output voltage 6 ms before the charge pulse.[13] The selected pulse shape of 2 $\mu$s length and nominal −30 mA height approximately matches the dimensions of a linac beam pulse of −60 nC. The voltage difference $\Delta U_{\text{out}}$ between before and after the charge pulse is determined from the y-axis intercepts of the linear fits to pre-pulse data from $t$ = −6 ms to −2 ms (blue line) and post-pulse data from $t$ = 14 ms to 34 ms (red line),[14] with the side condition that both have the same slope. By means of this procedure, constant offset currents are eliminated. Figure 7b shows the same data as in figure 7a with detail enlargement (y-axis break). The nonzero slope results from the offset current of the charge pulse generator. A negligence of this offset current may cause deviations of about 1 %. With the Faraday cup and a linac beam as charge source instead of the pulse generator at the electrometer input, the residua of the linear fit are almost one order of magnitude smaller and an offset current is not observable.

A low voltage at the input of the electrometer $U_{\text{in}}$ during a charge measurement approaches the regular conditions for the electrometer, the same as for its calibration with quasi-static charges. In order to ensure that $U_{\text{in}}$ remains sufficiently small even for large charge pulses, an additional capacitor (bipolar, polystyrene) is installed at the electrometer input ($C_{\text{in}}$ in figure 3). Figure 8a shows $U_{\text{in}}$ as a function of time for a 2 $\mu$s pulse with a nominal charge of $Q$ = −60 nC for an

[13]There is no significant influence (< 0.002 %) of $U_0$ on the charge measurement within the used range until the electrometer is discharged (0 V > $U_0$ > −100 V), i.e. the electrometer reacts linearly.

[14]The length of the post-pulse data is set to 20 ms in order to avoid possible effects from residual mains hum (50 Hz) on the determination of the slope.



2017 JINST 12 P03003

additional capacity of $C_{\mathrm{in}} = 33$ nF. During the period of the pulse from 0 to 0.002 ms the capacitor becomes charged by the nearly constant current resulting in a linear change of the voltage with a final value of $U_{\mathrm{in}}^0 = Q/C_{\mathrm{in}}$. Subsequently, the operational amplifier of the electrometer carries the charge on its feedback capacitor by minimizing the voltage at the input. This is observable as damped oscillation of $U_{\mathrm{in}}(t)$ (note the different time scale before and after the x-axis break). Due to the polarity inversion at this oscillation the additional capacitor has to be bipolar. The damped oscillation converges (approx. with $\exp(-t \cdot 1.5/\mathrm{ms})$) already within 7 ms after the pulse to less than 0.01 %. Since the output voltage $U_{\mathrm{out}}$ oscillates in the same manner, it converges within the same time span.[15] To be on the safe side, for the measurement of a converged output voltage difference $\Delta U_{\mathrm{out}}$ the evaluation of the post-pulse data does not start until 14 ms after the pulse (red line in figure 7). The "$10^{-7}$ C" measuring range of the electrometer is not used, since the damping of the oscillation is considerably slower, in particular if $C_{\mathrm{in}} > 20$ nF.

The value of the additional capacity $C_{\mathrm{in}}$ determines the initial input voltage after the charge pulse $U_{\mathrm{in}}^0$, i.e the extent of the deviation from the conditions during the calibration of the electrometer. Therefore the dependence of the electrometer signal on $C_{\mathrm{in}}$ is being studied. The electrometer signal in terms of a charge is

$$S_{\mathrm{E}} = N_{\mathrm{E}} \cdot \Delta U_{\mathrm{out}}. \tag{3.2}$$

Figure 8b shows the relative deviation of the mean electrometer signal $\langle S_{\mathrm{E}} \rangle$ from the charge pulse generator in each case from its asymptotic value at large $C_{\mathrm{in}}$ (low $U_{\mathrm{in}}^0$) as a function of $C_{\mathrm{in}}$. For pulses with nominal charges of −30 nC (squares), −60 nC (circles), and −120 nC (triangles), the relative deviations are similar. The observed asymptotic trend is a characteristic of the electrometer and not a reaction of the charge pulse generator to the voltage $U_{\mathrm{in}}^0$. A similar dependence on $C_{\mathrm{in}}$ is observed if the Faraday cup with a linac beam[16] is used as the source of charge pulses instead of the charge pulse generator (diamonds in figure 8b). For the used capacity of $C_{\mathrm{in}} = 33$ nF the deviation is about 0.02 % (upper dashed line). Together with the uncertainty of the asymptotic value, the contribution to the uncertainty due to the pulsed operation is estimated to be $u_{\mathrm{pulse}}(S_{\mathrm{E}})/S_{\mathrm{E}} = 0.03$ % for charge pulses in the range of −30 nC to −120 nC. This is dominant against the uncertainty contribution due to the calibration for quasi-static charge measurement $u_{\mathrm{cal}}(N_{\mathrm{E}})/N_{\mathrm{E}}$.

Some evidence for the proper elimination of radio-frequency interferences, mains hum, or noise due to ground loops can be checked by plotting the electrometer signals in a histogram. Figure 9a shows the $S_{\mathrm{E}}$ histogram for about 2000 sequent charge pulses of nominal −60 nC. The good agreement with a Gaussian function (red curve) reveals the random nature of the remaining noise at the readout of the electrometer output voltage difference $\Delta U_{\mathrm{out}}$. The width of the Gaussian in terms of $2\sigma$ (two standard deviations) corresponds to the precision ($k = 2$) of the measurement of a single charge pulse, i.e. the statistical contribution to its expanded absolute uncertainty due to the noise.

Figure 9b shows the widths of the best fit Gaussian functions to the $S_{\mathrm{E}}$ histograms at different values of the mean pulse charge. The width is independent of the pulse charge, in particular also at zero, i.e. if the pulsing of the generator is idle (zero signal). Thus pulse to pulse charge fluctuations

[15] The starting point of the post-pulse data (with 20 ms length) is varied from 9 ms to 34 ms without any significant effect (< 0.007 %) on the determined output voltage difference $\Delta U_{\mathrm{out}}$.

[16] Due to the charge fluctuations of the linac beam pulses the electrometer signal is normalized to the corresponding beam pulse charge simultaneously measured by means of the current transformer.



2017 JINST 12 P03003

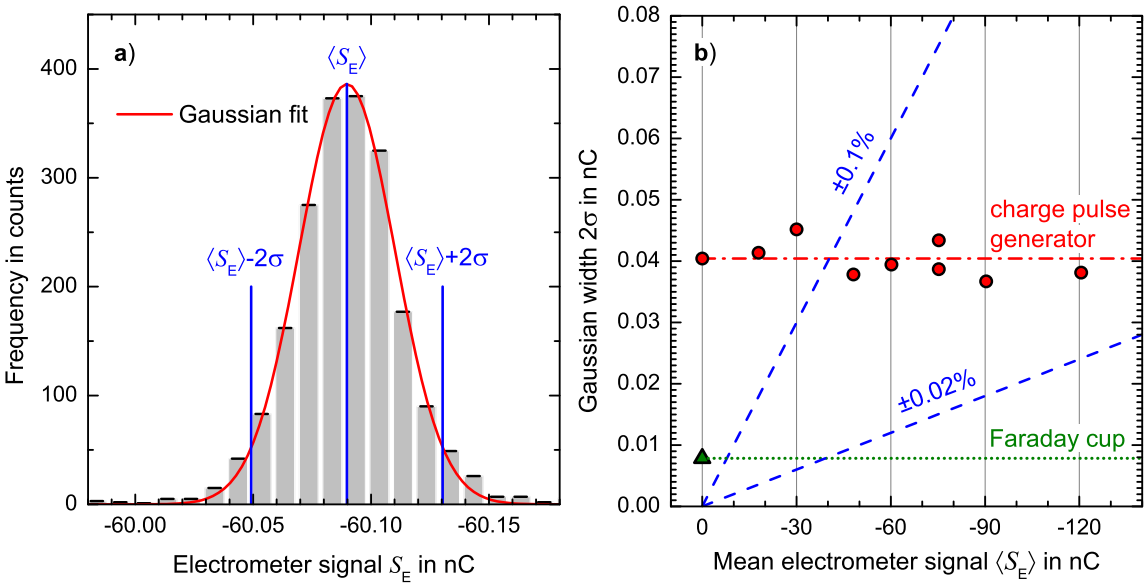


**Figure 9**. a) histogram of electrometer signals $S_E$ for about 2000 sequent charge pulses from the pulse generator at nominal −30 mA pulse height and 2 $\mu$s pulse length. Red curve: best fit of a Gaussian function. b) widths of the best fit Gaussian functions to the histograms of electrometer signals at different pulse charges from the pulse generator as a function of the mean electrometer signals $\langle S_E \rangle$, i.e. the center of the respective Gaussian. Blue dashed lines: limits for a precision of ±0.1 % or ±0.02 % ($k = 2$) as indicated. Red dash-dotted line: noise contribution if the electrometer is connected to the pulse generator. Green triangle: width of the $S_E$ histogram if the electrometer is connected to the Faraday cup. Green dotted line: noise contribution at the readout of the Faraday cup with the electrometer.

are negligible compared to the offset current noise, also for pulses with higher charges. The red dash-dotted line indicates the statistical contribution from the noise to the expanded uncertainty in the readout of the electrometer connected to the charge pulse generator $u^{cpg}_{stat}(S_E) = 0.04$ nC. The upper blue dashed line indicates the limit for a precision of 0.1 % ($k = 2$). It is obvious that a single charge pulse of about −60 nC can be measured with a precision better than 0.1 %. The resulting uncertainty contribution for the measurement of the mean charge of at least 500 pulses of −60 nC from the charge pulse generator is $u^{cpg}_{stat}(S_E)/S_E = 0.003$ %. Together with the nonstatistical uncertainty contributions, the combined expanded uncertainty amounts to $u^{cpg}_{c,mean}(S_E)/S_E = 0.031$ %.

If the electrometer is connected to the Faraday cup without a beam[17] the resulting uncertainty contribution for the measurement of charge pulses of about −60 nC is $u_{os}(S_E)/S_E = 0.004$ %. The width of the Gaussian fit to the corresponding histogram amounts to $2\sigma = 0.008$ nC. This is shown as a green triangle in figure 9b. Thus the green dotted line indicates the statistical contribution $u^{fc}_{stat}(S_E) = 0.008$ nC from the noise to the combined expanded uncertainty in the readout of the Faraday cup with the electrometer. The lower blue dashed line indicates the limit for a precision of 0.02 %. For the measurement of a single pulse charge of −60 nC from the Faraday cup the resulting statistical uncertainty contribution amounts to $u^{fc}_{stat}(S_E)/S_E = 0.013$ %. Together

[17]There is no significant difference if the beam is deflected in the beam dump or if the linac is switched off.



2017 JINST 12 P03003

with the nonstatistical uncertainty contributions, the combined expanded uncertainty amounts to $u^{\mathrm{fc}}_{\mathrm{c,single}}(S_{\mathrm{E}})/S_{\mathrm{E}} = 0.033\,\%$. Table 1 summarizes the contributions to the combined expanded relative uncertainty of the measurement of a single charge pulse of −60 nC from the Faraday cup or of the mean pulse charge from the charge pulse generator, respectively, by means of the electrometer.

**Table 1**. Contributions to the expanded relative uncertainty ($k = 2$) of the electrometer signal $S_{\mathrm{E}}$ for the measurement of a single charge pulse of about −60 nC from the Faraday cup or of the mean pulse charge from the charge pulse generator, respectively. The last column refers to the corresponding figures of the data on which the uncertainty estimation is based.

| | Uncertainty contribution | Type | Uncertainty in % | Figure |
|---|---|---|---|---|
| $u_{\mathrm{cal}}(N_{\mathrm{E}})$ | calibration for quasi-static charges | A | 0.0071 | 6 |
| $u_{\mathrm{pulse}}(S_{\mathrm{E}})$ | uncertainty due to pulsed operation | B | 0.03 | 8b |
| $u_{\mathrm{os}}(S_{\mathrm{E}})$ | uncertainty due to offset | B | 0.004 | |
| $u^{\mathrm{fc}}_{\mathrm{stat}}(S_{\mathrm{E}})$ | noise at readout of Faraday cup | A | 0.013 | 9b |
| $u^{\mathrm{cpg}}_{\mathrm{stat}}(S_{\mathrm{E}})$ | noise at readout of charge pulse generator[a] | A | 0.003 | 9b |
| $u^{\mathrm{fc}}_{\mathrm{c,single}}(S_{\mathrm{E}})$ | combined (single pulse from Faraday cup) | | 0.033 | |
| $u^{\mathrm{cpg}}_{\mathrm{c,mean}}(S_{\mathrm{E}})$ | combined (mean from pulse generator)[a] | | 0.031 | |

[a] For ≥ 500 pulses from charge pulse generator.

### 3.2 Current integrator and Waveform digitizer

In order to validate the accuracy of the electrometer, the determined pulse charges are compared with the results from a further measurement method, the determination of the mean pulse charge via the mean current by means of an Ortec 439 current integrator. This device sends one counting pulse to its digitized output every time the accumulated charge exceeds a discrete step of about −10 nC (at the used $10^{-8}$ C measuring range). In this manner it is not possible to measure precisely individual charge pulses of about −60 nC. However the mean charge of many pulses can be determined with sufficient accuracy. For the measurement of the mean current a counter (Agilent 53220A) counts the total number of counting pulses $n_{\mathrm{out}}$ from the digitized output within an accurately defined time span $\Delta t$. The mean current is then given by

$$I_{\mathrm{CI}} = N_{\mathrm{CI}} \cdot n_{\mathrm{out}}/\Delta t, \tag{3.3}$$

where $N_{\mathrm{CI}}$ is the calibration coefficient of the current integrator. The time span is chosen to be $\Delta t = 2000/f_{\mathrm{P}}$ so that 2000 charge pulses are always integrated independent of the pulse repetition rate $f_{\mathrm{P}}$. Thereby, effects from the −10 nC discretization are < 0.01 % for charge pulses with −60 nC.

The determination of the calibration coefficient (of the used $10^{-8}$ C/count range) is carried out by the measurement of the mean frequency $f_{\mathrm{out}}$ at the digitized output (30 Hz to 10 kHz) when a stable reference current of 0.3 $\mu$A to 100 $\mu$A is fed in the input. The reference currents $I_{\mathrm{ref}} = U_{\mathrm{ref}}/R_{\mathrm{ref}}$ are generated by means of temperature stable high precision resistors (Caddock USF 340, specified tolerance 0.01 %, verified) with $R_{\mathrm{ref}}$ between 20.00 MΩ and 0.5 MΩ and a reference voltage $U_{\mathrm{ref}}$ between −5 V and −100 V from a voltage source (HP3245A). The calibration



2017 JINST 12 P03003

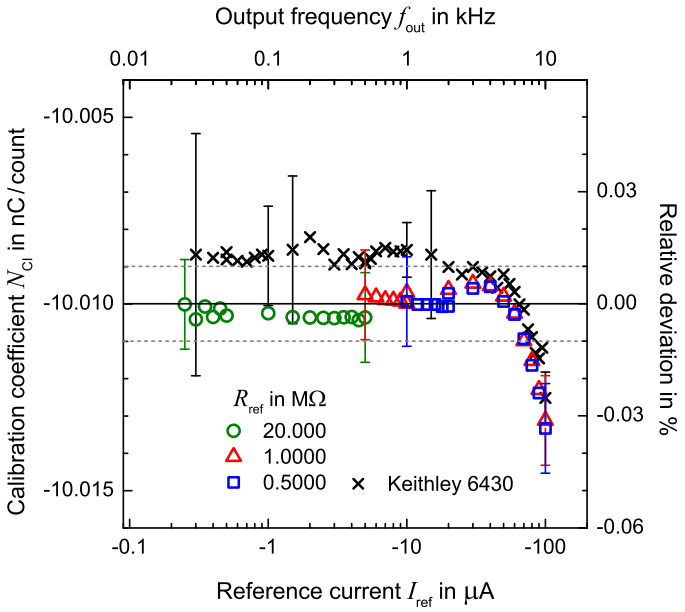


**Figure 10**. Calibration coefficient $N_{CI}$ of the Ortec 439 current integrator in the "$10^{-8}$ C" range as a function of the reference current generated with $R_{ref}$ = 20.000 MΩ (circles), 1.0000 MΩ (triangles), and 0.5000 MΩ (squares). Right y-axis: deviation from the mean value at $-2\ \mu A > I_{ref} > -60\ \mu A$. Upper x-axis: corresponding output frequency $f_{out}$. Crosses: results from utilization of a Keithley 6430 current source. Dashed lines: limits for ±0.01 % deviation. For reasons of clarity, error bars are shown only for lowest and largest value per resistor or measurement range, respectively.

coefficient is given by

$$\begin{aligned} N_{CI} &= I_{ref}/f_{out} \\ &= U_{ref}/R_{ref}f_{out}\,. \end{aligned} \tag{3.4}$$

Figure 10 shows the obtained calibration coefficient as a function of the reference current using three different high-ohmic resistors as indicated (open symbols). The results agree within ±0.01 % (dashed lines). The right y-axis indicates the relative deviation from the mean value for currents $-0.3\ \mu A > I_{ref} > -60\ \mu A$. In this range the calibration coefficient is independent of the current. From $-60\ \mu A$ on, the saturation effect becomes apparent. This corresponds to an output frequency $f_{out} > 6$ kHz (upper x-axis). The deviation from the nominal value of 10 nC/count amounts to approx. 0.1 %.[18] The determined calibration coefficient varies slightly (some 0.01 %) from day to day due to temperature effects.[19] Through calibration shortly before or after each series of measurements, effects due to fluctuations in temperature are reduced to below 0.005 %. The expanded uncertainty of the calibration coefficient, taking into account the specified resistor tolerance and residual effect due to temperature fluctuations, is estimated to be $u(N_{CI})/N_{CI} = 0.013$ %.

[18]The Ortec 439 is calibrated at first operation by potentiometers on the circuit board. The in situ determination of a calibration coefficient takes into account drifts as, e.g., due to fluctuations in temperature.

[19]The temperature stability as specified by the manufacturer is 0.05 %/°C.



2017 JINST 12 P03003

In order to exclude effects from unconsidered additional resistances or offset voltages on the current source made of the high-ohmic resistor and the voltage source, a Keithley 6430 current source is used complementarily for the generation of $I_{\mathrm{ref}}$.[20] Since the accuracy of the nominal current of the Keithley 6430 is insufficient,[21] the output current is measured by an amperemeter (Agilent 3458A). The obtained calibration coefficients are shown in figure 10 as crosses. The expanded uncertainty of the mean value (at $f_{\mathrm{out}} < 6$ kHz), taking into account the specified uncertainty of the amperemeter, is estimated to be $u(N_{\mathrm{CI}})/N_{\mathrm{CI}} = 0.007$ %. The mean value agrees with the calibration coefficient from the calibration by means of the resistors (deviation < 0.012 %) within the combined uncertainty budget. Thus significant effects due to errors of the current made by means of the high-ohmic resistors can be excluded.

The routine calibrations shortly before or after each series of measurements are carried out with five different currents by means of the 20.00 MΩ resistor. The expanded uncertainty of the determined calibration coefficient is estimated to be $u_{\mathrm{cal}}(N_{\mathrm{CI}})/N_{\mathrm{CI}} = 0.013$ %.

For the measurement of charge pulses of up to −120 nC, a 15 $\mu$F capacitor (Vishay MKP1848) is installed in parallel, and a resistor $R_{\mathrm{in}} = 120\ \Omega$ in series, at the input of the current integrator (see figure 3).The capacitor acts as a storage element for the charge until the current integrator processes it and at the same time keeps the voltage at the input below the rated maximum of 10 mV [29]. The resistor limits the maximal current in order to avoid saturation effects for currents < −60 $\mu$A ($f_{\mathrm{out}} > 6$ kHz). Without the resistor deviations up to −0.1 % are observed. A further increase of the capacity at the input > 15 $\mu$F (with 120 Ω at the input) does not affect the results. The uncertainty contribution due to effects owing to the pulsed operation is estimated to be $u_{\mathrm{pulse}}(N_{\mathrm{CI}})/N_{\mathrm{CI}} = 0.01$ %.

The current $I_{\mathrm{CI}}$ as given by eq. (3.3) includes any offset current of the charge source. This may gives rise to considerable deviations in the integrated charge per charge pulse $Q_{\mathrm{CI}} = I_{\mathrm{CI}}/f_{\mathrm{P}}$ calculated from the measured mean current $I_{\mathrm{CI}}$ and the pulse repetition rate $f_{\mathrm{P}}$ from the actual pulse charge. Even though the pulse generator features only a very small offset current (< 0.0001 % of the pulse amplitude of −30 mA), at $f_{\mathrm{P}} = 5$ Hz about −4 nC of $Q_{\mathrm{CI}}$ originates from the integration of the continual offset current between the charge pulses. This corresponds to approx. 7 % deviation for a −60 nC pulse. Since the offset current is independent of the charge pulse repetition rate $f_{\mathrm{P}}$, it can be eliminated by the variation of $f_{\mathrm{P}}$. The symbols in figure 11a represent the mean currents $I_{\mathrm{CI}}$ as a function of $f_{\mathrm{P}}$ for 2000 charge pulses in each case for four different values of pulse charge from the charge pulse generator. The current integrator signal in terms of a charge without a contribution from an offset current results from the slope $S_{\mathrm{CI}}$ of the linear fit in each case (lines). Residual effects due to the −10 nC discretization are mostly canceled out on average (eight data points per fit). The axis intercept, i.e. the offset current, is about $I_0 = -19$ nA in all cases. The residua from the linear fit lines are less than 0.03 %. The standard uncertainty of the slope of the linear fit is about 0.001 nC in each case (<0.002 % of −60 nC).

Figure 11b shows the deviation $(S_{\mathrm{CI}}/\langle S_{\mathrm{E}}\rangle) - 1$ of the mean pulse charge determined by means of the current integrator $S_{\mathrm{CI}}$ from the corresponding mean electrometer signal $\langle S_{\mathrm{E}}\rangle$ for the same pulse charge from the charge pulse generator in each case. The pulse charge is varied (in the range of 0.5 to 2 times the −60 nC to be measured) by the variation of the current amplitude

[20] As load, a resistor (120 Ω) is connected in series between the Keithley 6430 and the Ortec 439.

[21] Increasing deviations with decreasing current and jumps between the current ranges (0.04 %) are observed (within specified uncertainties).



2017 JINST 12 P03003

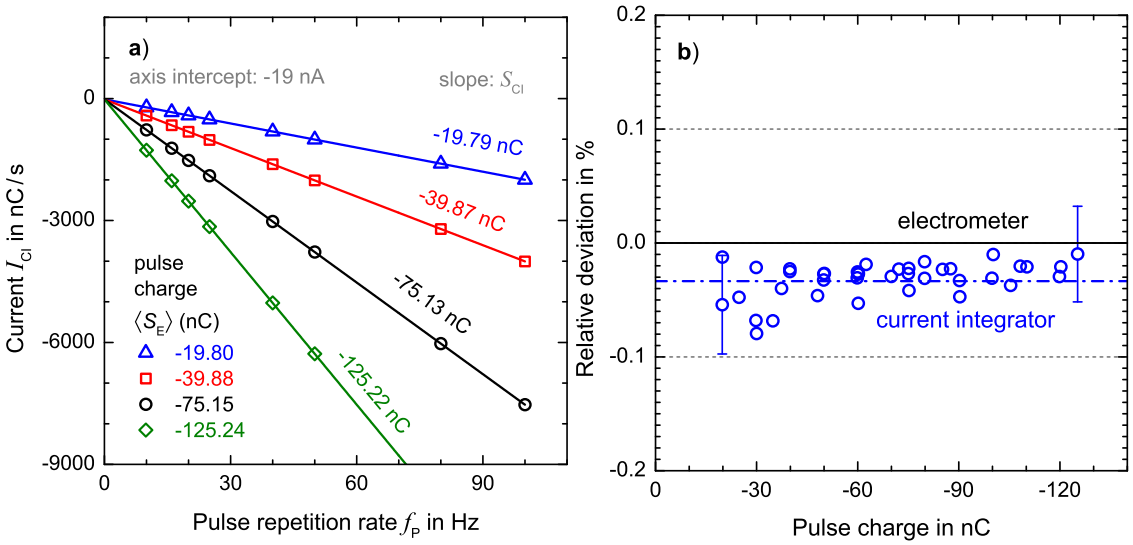


**Figure 11**. a) mean current $I_{CI}$ as recorded by the current integrator as a function of the pulse repetition rate $f_P$ of the charge pulse generator for four different values of the pulse charge. Pulse charge specification: mean pulse charge $\langle S_E \rangle$ as measured with the electrometer. Lines: linear fits with resulting slopes $S_{CI}$ as indicated and resulting axis intercept of about −19 nC/s in each case. b) deviation $(S_{CI}/\langle S_E \rangle) - 1$ of the pulse charge measured by the current integrator $S_{CI}$ from the result of the measurement with the electrometer $\langle S_E \rangle$ for the same pulse charges from the pulse generator in each case. For reasons of clarity, error bars are shown only for lowest and largest pulse charge.

between −10 mA and −60 mA and the pulse lengths between 1 $\mu$s and 3.5 $\mu$s. The deviations are independent of the charge in the studied range of pulse charges. The standard deviation amounts to 0.016 %. The resulting statistical contribution to the expanded uncertainty of the measurement of the mean pulse charge (2000 pulses at 8 different $f_P$) is $u^{cpg}_{stat}(S_{CI})/S_{CI} = 0.032$ %. Together with the nonstatistical uncertainty contributions, the combined expanded uncertainty amounts to $u^{cpg}_{c,mean}(S_{CI})/S_{CI} = 0.036$ %. The mean relative deviation amounts to about −0.03 % (dash-dotted line) which is within the combined uncertainty budget of the electrometer and the current integrator (0.035 %). Table 2 summarizes the contributions to the expanded relative uncertainty for the determination of the mean pulse charge from the charge pulse generator by means of the current integrator.

**Table 2**. Contributions to the expanded relative uncertainty ($k = 2$) for the determination of the mean pulse charge $S_{CI}$ from the charge pulse generator by means of the current integrator . The last column refers to the corresponding figures of the data on which the uncertainty estimation is based.

| | Uncertainty contribution | Type | Uncertainty in % | Figure |
|---|---|---|---|---|
| $u_{cal}(N_{CI})$ | calibration for constant currents | B | 0.013 | 10b |
| $u_{pulse}(S_{CI})$ | due to pulsed operation | B | 0.01 | |
| $u^{cpg}_{stat}(S_{CI})$ | statistical contribution | A | 0.032 | 11b |
| $u^{cpg}_{c,mean}(S_{CI})$ | combined | | 0.036 | |



2017 JINST 12 P03003

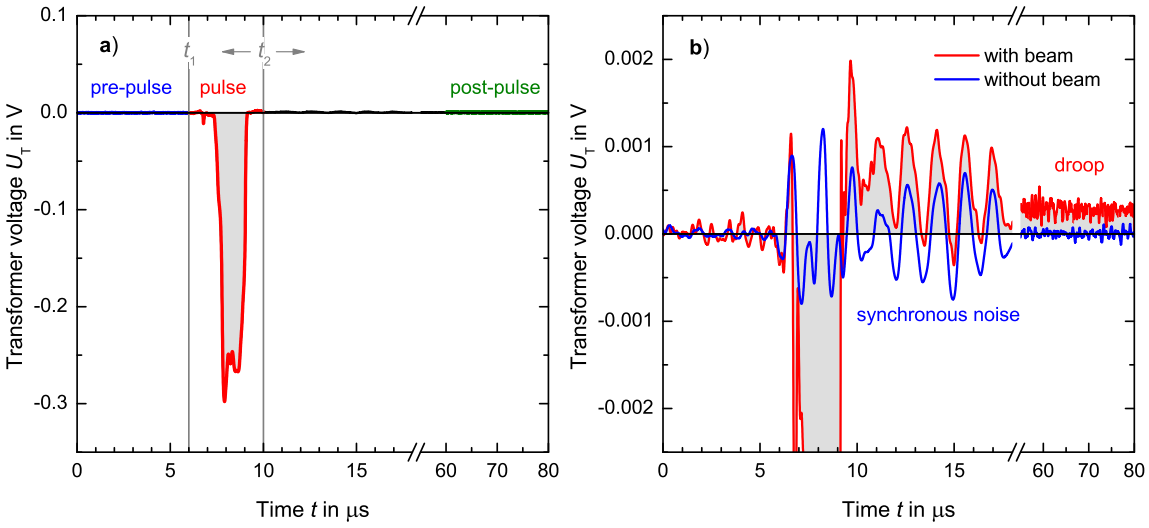


**Figure 12**. a) transformer voltage $U_T$ as a function of time with respect to the linac trigger for a beam pulse of approx. −71 nC. $t_1$ and $t_2$: pulse integration limits. b) red curve: same data as in figure 12a but with detail enlargement. Blue curve: synchronous noise from operating linac without beam passing through the ICT.

For a consistency check of the pulse-resolved charge measurement, the results from the electrometer are compared to the results of a further independent method, the measurement of the time-resolved pulse current. The voltage drop across a temperature-stable high precision measuring resistor with $R_{MR}$ = 50.000 Ω (Vishay RCK02, 0.001 % tolerance, verified) is recorded by means of the 14-bit waveform digitizer (connector 3 in figure 3). The mean deviation of all measurements with the waveform digitizer from the electrometer amounts to 0.04 %, which is within the combined uncertainty budget of the waveform digitizer and the electrometer (0.06 %).

In conclusion, since the results of the three independent measuring methods by means of the electrometer, the current integrator, and the waveform digitizer are consistent, there are no indications of significant errors at the measurement of pulsed charges with the electrometer or of deviations from its estimated uncertainty.

## 4 Current transformer

For the accurate nondestructive measurement of the beam pulse charge by means of the beam intensity monitoring system consisting of the ICT, the preamplifier, the transmission cable, and the waveform digitizer, two procedures are necessary. The first one is the preparation of a monitor signal acquisition without significant noise contributions. This includes, in particular, the elimination of synchronous noise, induced by interferences emitted from the running linac, which arise synchronously with the beam pulse. And the second one implies the calibration of the monitor signal against the corresponding charge from the Faraday cup which is measured traceable to primary standards by the methods described in the previous section.



2017 JINST 12 P03003

### 4.1 Signal acquisition

Figure 12 shows the transformer voltage $U_T(t)$ from the preamplifier connected to the output of the ICT for a typical linac beam pulse as a function of time with respect to the linac trigger (at $t = 0$), as recorded by the waveform digitizer. The baseline offset, caused, among other things, by the adjustable offset of the preamplifier, is determined from the mean voltage of the pre-pulse data at $0 < t < t_1$ (blue curve). The determined offset is already subtracted in $U_T(t)$. The voltage-time integral of the ICT output pulse (red curve) is proportional to the charge of the inducing beam pulse. By applying the transformer equations, one receives the transformer signal in terms of a charge

$$S_T = \frac{n_T}{n_G R_T} \int_{t_1}^{t_2} U_T(t) \mathrm{d}t \tag{4.1}$$

where $n_T = 50$ is the nominal number of turns of the transformer winding, $R_T = 25\ \Omega$ is the nominal load impedance of the transformer (50 Ω embedded in the ICT and 50 Ω termination at the input of the preamplifier connected in parallel), and $n_G = 10$ is the nominal gain of the preamplifier (20 dB). Thus the nominal sensitivity of the ICT in combination with the 20 dB preamplifier is $\epsilon = n_T/n_G R_T = 0.2$ C/Vs. The integration limits $t_1 = 6\ \mu$s and $t_2$ contain the pulse edges. The transformer voltage peak ends at $t \approx 9.3\ \mu$s, where $U_T$ becomes positive. Therefore $t_2 \geq 9.3\ \mu$s is a reasonable choice.

Since the ICT works as a classical alternating current transformer, it cannot transmit a direct current component, i.e. the transformer voltage $U_T(t)$ must have positive and negative portions of equal area [16]. Therefore a positive transformer voltage is present after the negative pulse. Its height depends on the droop time constant of the transformer [15, 19, 20] as well as on the shape and length of the negative pulse. Effects in a train of successive pulses due to the remaining signal droop from the previous pulse are negligible here even at the highest repetition rate (100 Hz). They are anyway eliminated by the determination of the baseline offset before each pulse. The effect of the signal droop can be determined from post-pulse data at $60\ \mu\text{s} < t < 80\ \mu$s (green curve in figure 12a), where all contributions from the beam pulse and the synchronous noise emitted from the running linac have vanished. This is obvious in the red curve in figure 12b, which shows the data from figure 12a with detail enlargement. For comparison, the zero signal with the synchronous noise from the running linac is plotted (blue curve). It is measured by deflecting the beam into the beam dump ("D" in figure 1) instead of in the beamline and thus without the beam passing through the ICT. The synchronous noise disappears if the klystron and, by implication, the actual interfering transmitters, the modulator and the high voltage generator are switched off. It superimposes the voltage pulse from the ICT. Due to the signal droop, the tail of $U_T(t)$ after the negative beam pulse is shifted up to positive voltages. Therefore the choice of the integration limit $t_2$ in eq. (4.1) influences the value of the transformer signal $S_T$ as discussed below in section 4.2.

Noise picked up on transmission cables is a persistent problem in systems forced to operate in an accelerator environment [30, 31]. The synchronous noise from the running linac may result in an offset $b_1$ to the transformer signal $S_T$. The effect is considerably more pronounced if the grounding of the ICT is connected to the grounding of the beamline and thus to the grounding of the linac. Then offsets of up to 0.6 nC (1 % of 60 nC) are observed, depending on the actual cabling and the electromagnetic environment. An advantage of transformers is that both ends of the secondary winding can be left floating. Unfortunately, at the used in-flange ICT one end of the secondary



2017 JINST 12 P03003

winding is internally connected to the flange body (SMA output connector with grounded shield) and thus to its grounding. In order to nevertheless realize a floating connection with respect to the beamline grounding, as proposed in refs. [32] and [20], the ICT is mounted galvanically isolated from the beamline between two vacuum ceramic breaks ("C" in figure 2b). Then at $t_2 = 9.3\ \mu$s the offset $b_1$ is negligible (< 0.005 nC). Furthermore, voltage fluctuations due to a ground loop are avoided this way.[22] The expanded uncertainty for the determination of the offset (for the galvanically isolated ICT) is estimated to be $u(b_1) = 0.005$ nC.

Ordinary split (snap-on) ferrite cores usually installed at transmission cables do not measurably influence the effect of the synchronous noise, neither for the isolated nor for the grounded ICT. However, recent test reveal that with a filter composed of a RG58 cable winded ten times around a potcore ferrite (TDK PM 50/39, B65646) the residual synchronous noise of the isolated ICT can be strongly attenuated.

The effect of the random noise from the waveform digitizer and the preamplifier on the precision of the transformer signal increases linearly with the length of the integration interval. For $t_2 = 9.3\ \mu$s the precision amounts to about ±0.03 nC. Thus the statistical contribution to the expanded relative uncertainty of the measurement of the charge of a single beam pulse of about −60 nC amounts to $u_{\mathrm{stat}}(S_\mathrm{T})/S_\mathrm{T} = 0.05$ %.

### 4.2 Calibration

The transformer signal $S_\mathrm{T}$ may deviate from the beam pulse charge due to the voltage loss at the resistance of the coaxial cable between the preamplifier at the ICT and the waveform digitizer (1.34 Ω, −2.7 % deviation), due to the cable between ICT and preamplifier (−0.1 %), due to the signal droop of the ICT (nominal < 2 %/$\mu$s), due to the gain accuracy of the preamplifier ((20 ± 0.2) dB, ±2.3 %), due to the gain error of the waveform digitizer (±0.1 %), due to eddy current loss in the transformer core (nominal < 1 %), and due to signal deformations by the dispersive properties of the coaxial cable. For an accurate measurement of the charge of the beam pulses by means of the ICT the transformer signal is calibrated against the pulse charge collected by the Faraday cup. The charge measurement is traceable to primary standards as described in section 3. The correction with respect to the finite collection efficiency of the Faraday cup is described in section 5. The transformer signal $S_\mathrm{T}$ and the Faraday cup signal $S_\mathrm{FC}$ of a beam pulse are acquired and evaluated simultaneously in real time. In order to ensure a clear assignment of $S_\mathrm{T}(i)$ to $S_\mathrm{FC}(i)$ a stand-alone counter counts the pulse numbers $i$ in real time. The current number $i$ is verified at the beginning and at the end in the $S_\mathrm{T}$ and $S_\mathrm{FC}$ evaluation routines via Ethernet LAN communication with the counter (see figure 3).

The blue dots in figure 13a represent the transformer signals $S_\mathrm{T}$ (to be calibrated) of about 500 sequent single beam pulses as a function of the simultaneously collected corresponding charge from the Faraday cup at stable operation of the linac. The Faraday cup signal is measured by means of the electrometer $S_\mathrm{FC} = S_\mathrm{E}$ (connectors 1 to 4 in figure 3). Thus the relative uncertainty is $u(S_\mathrm{FC}) = u^{\mathrm{fc}}_{\mathrm{c,single}}(S_\mathrm{E}) = 0.0033$ %. The red line results from a linear fit $S_\mathrm{T} = m \cdot S_\mathrm{FC} + b$. The dashed line indicates the equality $S_\mathrm{T} = S_\mathrm{FC}$ and visualizes the deviation to be corrected by the

[22] The beamline grounding forms a second grounding point in addition to the grounding of the waveform digitizer which results in offset voltage fluctuations due to a ground loop.



2017 JINST 12 P03003

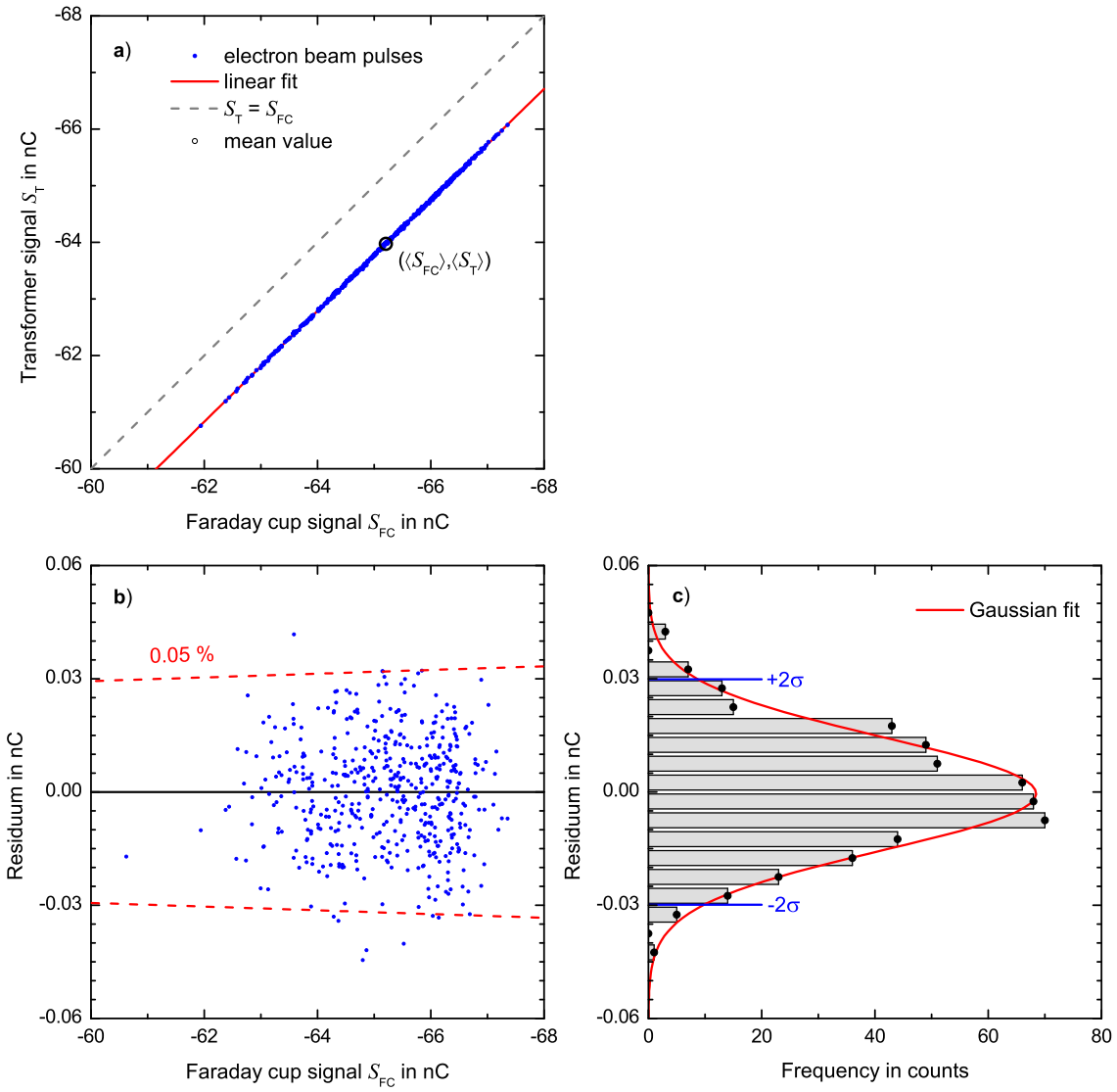


**Figure 13**. a) transformer signal $S_T$ (at $t_2 = 9.3\ \mu s$) of about 500 sequent single beam pulses as a function of the simultaneously collected corresponding charge $S_{FC}$ from the Faraday cup at stable operation of the linac. Red line: linear fit. Dashed line: $S_T = S_{FC}$. Open circle: mean value $(\langle S_{FC}\rangle, \langle S_T\rangle)$. b) residua of the linear fit function. Dashed red line: limits for a residuum within ±0.05 %. c) histogram of the residua. Red curve: best fit of a Gaussian distribution.

calibration factor. Figure 13b shows the residua of the linear fit ($m \cdot S_{FC} + b - S_T$). The scattering within ±0.03 nC arises mainly from the noise at the readout of the current transformer in agreement with the statistical uncertainty of $u_{stat}(S_T)/S_T = 0.05$ % (dashed red lines) estimated in section 4.1. The noise at the readout of the Faraday cup by means of the electrometer is about four times less ($2\sigma = 0.008$ nC) and thus contributes only marginally to the combined statistical uncertainty. The residua are randomly distributed which is obvious in the Gaussian shape of the corresponding histogram shown in figure 13c. The width of the Gaussian fit (red curve) amounts to $2\sigma = 0.03$ nC. Thus the statistical contribution to the expanded relative uncertainty of the measurement of the charge of a single beam pulse of about −60 nC amounts to $u_{stat}(S_T)/S_T = 0.05$ %.



2017 JINST 12 P03003

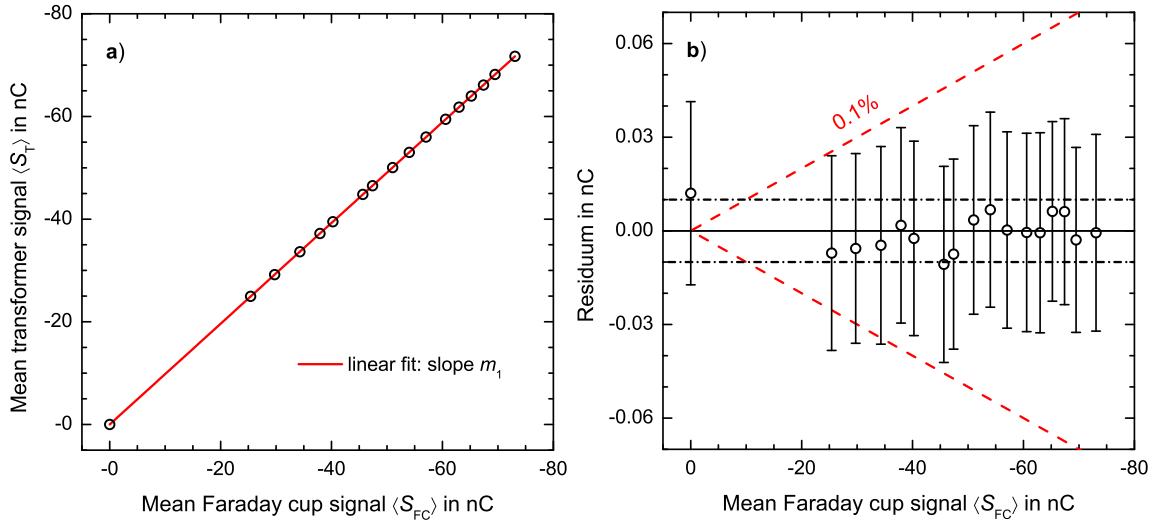


**Figure 14**. a) mean transformer signal $\langle S_T \rangle$ as a function of the mean Faraday cup signal $\langle S_{FC} \rangle$ for different beam intensities for about 500 beam pulses at each data point. Integration limit $t_2 = 9.3\ \mu s$. Red Line: linear fit. b) residua from the linear fit. Bars denote the widths ($\pm 2\sigma$) of the Gaussian fits to the histograms of residua as shown in figure 13c, i.e. the precision ($k = 2$) for the measurement of a single pulse. Red dashed line: limits for a residuum of ±0.1 %.

The linearity of the ICT is specified by the manufacturer as < 0.1 %. The linearity of the entire beam intensity monitoring system is verified in the applied pulse charge range by varying the intensity of the beam. For reasons of clarity, only the mean values at each intensity setting are considered in the following since the points $(\langle S_{FC} \rangle, \langle S_T \rangle)$ lie exactly on the line of the linear fit in each case ($m \cdot \langle S_{FC} \rangle + b = \langle S_T \rangle$), as shown, for example, in figure 13a as an open circle. Figure 14a shows the mean transformer signal $\langle S_T \rangle$ as a function of the mean Faraday cup signal $\langle S_{FC} \rangle$ for different beam intensities. The red line results from a linear fit of $\langle S_T \rangle = m_1 \cdot \langle S_{FC} \rangle + b_1$. The calibration factor $N_T = 1/m_1$ of the beam intensity monitoring system is obtained from the slope $m_1$. From the variance of the slope a relative uncertainty contribution of 0.016 % ($k = 2$) is calculated. Together with the nonstatistical uncertainty contributions of the electrometer reading (table 1), the combined expanded uncertainty of the calibration factor is $u_{cal}(N_T)/N_T = 0.035$ %. The axis intercept $b_1$ is the correction for the offset due to the synchronous noise emitted from the linac. The transformer signal calibrated with respect to the Faraday cup signal is given by

$$\begin{aligned} \hat{S}_T &= S_{FC} \\ &= N_T \cdot (S_T - b_1). \end{aligned} \tag{4.2}$$

Figure 14b shows the residua ($\langle \hat{S}_T \rangle - \langle S_{FC} \rangle$) of the mean transformer signal from the linear fit function. A systematic linearity error is not observable. The residua are within ±0.01 nC (dash-dotted lines). Thus the resulting contribution to the relative uncertainty ($k = 2$) due to the nonlinearity of the entire beam intensity monitoring system for the measurement of a charge pulse of about −60 nC is estimated to be $u_{nl}(\hat{S}_T)/\hat{S}_T = 0.017$ %.



2017 JINST 12 P03003

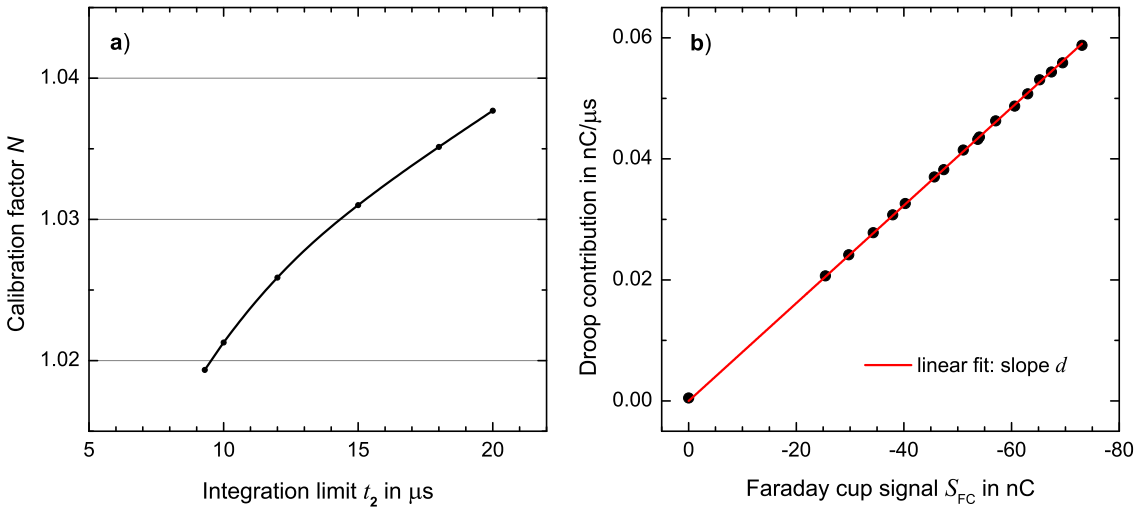


**Figure 15**. a) calibration factor $N_T$ as a function of the integration limit $t_2$. b) contribution of the droop effect to the transformer signal in terms of charge per integration time as a function of the Faraday cup signal.

From the uncertainty of the offset ($u(b_1) = 0.005$ nC) the contribution to the relative uncertainty ($k = 2$) due to the synchronous noise for the measurement of a pulse of about −60 nC is estimated to be $u_{sn}(\hat{S}_T)/\hat{S}_T = 0.008$ %. The offset $b_1$ may change with the electromagnetic environment and the actual cabling. Therefore it should be newly acquired for checkup at every utilization of the ICT. For this checkup the Faraday cup does not need to be present. It is sufficient to measure the zero signal of $S_T$ at the running linac.

The bars in figure 14b denote the measured widths in terms of $2\sigma$ of the Gaussian fits to the histograms of the residua as shown in figure 13c.[23] Thus the bars represent the statistical contribution $u_{stat}(\hat{S}_T)$ to the expanded absolute uncertainty of the measurement of a single charge pulse due to the noise. The red dashed lines indicate the limits for a residuum within ±0.1 %. Thereby it becomes obvious that for every single charge pulse in the range of interest of (−60 ± 10) nC the calibrated transformer signal $\hat{S}_T$ agrees with the Faraday cup signal $S_{FC}$ clearly better than ±0.1 %. As discussed above, the statistical contribution to the expanded relative uncertainty of the measurement of a single beam pulse of about −60 nC amounts to $u_{stat}(\hat{S}_T)/\hat{S}_T = 0.05$ %.

The transformer signal $S_T$ and thus the respective calibration factor $N_T$ depend on the integration limit $t_2$ due to the signal droop, i.e. a transformer voltage $U_T > 0$ after the negative pulse as readily identifiable in figure 12b. This results in a decrease in the absolute value of $S_T(t_2)$ with increasing $t_2$. Therefore the corresponding calibration factor $N_T(t_2)$ plotted in figure 15a increases with $t_2$. The difference from unity at $t_2 = 9.3$ µs results mainly from the voltage loss due to the resistance of the transmission cable between the preamplifier at the ICT and the waveform digitizer (−2.7 %) in combination with the finite collection efficiency of the Faraday cup (+0.8 %) as discussed in detail in section 5. The contribution of the signal droop within the integration interval can be determined

[23]The error bars (with respect to the statistical uncertainty) of the shown mean values (> 500 charge pulses in each case) are smaller than the size of the circle symbols.



2017 JINST 12 P03003

from mean transformer voltage $U_T$ at 60 $\mu$s $< t <$ 80 $\mu$s (post-pulse data, see figure 12). The droop contribution in terms of a charge per integration interval length is shown in figure 15b as a function of the Faraday cup signal which is proportional to the actual parameter of the signal droop, the transformer voltage pulse height. From the slope $d$ of the linear fit (red line) the droop effect is determined to be 0.08 %/$\mu$s. Thus a delay of the beam pulse or a time displacement of the integration interval by, for example, 125 ns results in 0.01 % deviation. Therefore the actual cabling for the trigger signals is part of the beam intensity monitoring system to be calibrated. Since the droop contribution is proportional to the Faraday cup signal, the effect is fully included in the calibration factor $N_T(t_2)$ and no further corrections (and uncertainty contributions) are necessary in eq. (4.2). However, if the shape of the pulse differs considerably from the pulse shape during the calibration, a modified droop effect may result in deviations. In future it will be possible to move the Faraday cup in situ into and out of the beam by means of an in-vacuum manipulator for periodic verification and in order to instantly recalibrate the transformer signal against the Faraday cup when the beam parameters are changed.

In order to avoid pulse shape depended effects due to the droop the measured transfer function of the ICT can be utilized. The transfer function is calculated as the quotient of the discrete Fourier transform (DFT) of a time-resolved test pulse ducted through the ICT and the DFT of the corresponding time-resolved ICT response. The test pulse can either produced with the charge pulse generator and fed in the Q-loop or beam pulses are utilized. For the latter case the DFTs of the Faraday cup current and the simultaneously recorded ICT current as shown in figure 5 are used. With the obtained transfer function it is possible to deconvolve the transformer voltage curve in order to get rid of the droop contribution and to restore the pulse shape as it would be measured by means of the Faraday cup. The deconvolved transformer signal should be invariant to the actual pulse shape and integration limit $t_2$. For a previously used ICT model (turns ratio of 5:1) with a nominal droop of $< 20$ %/$\mu$s this deconvolution procedure reduces the resulting uncertainty contribution. To which extent the method can improve the accuracy of the currently used ICT model with one order of magnitude smaller nominal droop is the scope of more detailed studies in future.

In conclusion, the beam intensity monitoring signal is calibrated against the corresponding charge from the Faraday cup. Thus sources for deviations such as, e.g., due to the voltage losses by the used transmission cables or due to the signal droop of the current transformer are included by the calibration coefficient. Table 3 summarizes the contributions to the expanded relative uncertainty of the transformer signal calibrated to the Faraday cup signal $\hat{S}_T$ for the measurement of a single beam pulse of approx. $-60$ nC. The required correction with respect to the finite collection efficiency of the Faraday cup for the determination of the actual pulse charge $Q_P$ from $\hat{S}_T$ is described in the next section.

## 5 Faraday cup collection efficiency

The calibrated transformer signal $\hat{S}_T$ equals the charge collected by the Faraday cup $S_{FC}$ but still differs from the desired actual pulse charge due to the finite collection efficiency of the Faraday cup. A Faraday cup for high-energy electrons may suffer from penetration losses, i.e. due to the incomplete stopping of the incident electrons or the insufficient encapsulation of the subsequent electromagnetic cascade, and backscatter losses, i.e. when backscattered electrons near the surface escape the Faraday cup. Losses due to current leakage have to be avoided by a sufficient insulation



2017 JINST 12 P03003

**Table 3**. Contributions to the expanded relative uncertainty ($k = 2$) of the transformer signal calibrated to the Faraday cup signal $\hat{S}_T$ (without taking into account the finite collection efficiency of the Faraday cup) for the measurement of a single beam pulse of approx. −60 nC by means of the beam intensity monitoring system. The last column refers to the corresponding figures of the data on which the uncertainty estimation is based.

| | Uncertainty contribution | Type | Uncertainty in % | Figure |
|---|---|---|---|---|
| $u_{cal}(N_T)$ | calibration against Faraday cup[a] | B | 0.035 | 14a |
| $u_{nl}(\hat{S}_T)$ | nonlinearity of the entire system | B | 0.017 | 14b |
| $u_{sn}(\hat{S}_T)$ | due to synchronous noise[b] | B | 0.008 | |
| $u_{stat}(\hat{S}_T)$ | statistical contribution[c] | A | 0.05 | 13c |
| $u_c(\hat{S}_T)$ | combined | | 0.063 | |

[a] For Faraday cup readout by means of the electrometer.
[b] For the galvanically isolated ICT.
[c] For $t_2 = 9.3\ \mu$s for the galvanically isolated ICT.

which have to be tested periodically. Since the losses of the Faraday cup are of the magnitude of the uncertainty strived for, a correction with respect to the collection efficiency is necessary. Since the collection efficiency is > 99 %, for the determination of the losses an uncertainty of < 5 % is sufficient in order to reach an uncertainty contribution < 0.05 %.

Additional deviations may become significant if the aperture of the Faraday cup is too small to catch the complete beam including its tails. Furthermore, at high-energy electron beams, small fractions from the beam tail which hit parts of the beamline may induce a significant portion of secondary electrons, in particular if the beam is not sufficiently aligned. The transformer and the Faraday cup may detect different fractions of these secondary electrons which may result in an error in the calibration or in the determination of the collection efficiency.

The collection efficiency is determined experimentally by a cancellation measurement as described hereafter in subsection 5.1. The results from a test on the influences of the beam alignment are given in subsection 5.2. Finally, the experimental results are compared with the results from a MC simulation in subsection 5.3.

### 5.1 Cancellation measurement

The collection efficiency of the Faraday cup is determined by a cancellation measurement as proposed by Pruitt [16]. It is based on a comparison of the beam current, measured by means of the transformer, with the current from the Faraday cup measured by the same transformer. The Faraday cup current is fed back through the ICT via the Q-loop in opposite direction to the beam into a 50 Ω terminating resistance (see figure 3).[24] The effects of the electron beam current and the counteracting current from the Faraday cup (see figure 5) on the ICT are canceled out if both are equal, i.e. if all electrons of the beam pulse are caught by the Faraday cup without losses. Otherwise a residual transformer signal results which can be used for the determination of the Faraday cup collection efficiency as described in the following.

[24] The cabling is such that it does not connect the ICT grounding with the beamline grounding.



2017 JINST 12 P03003

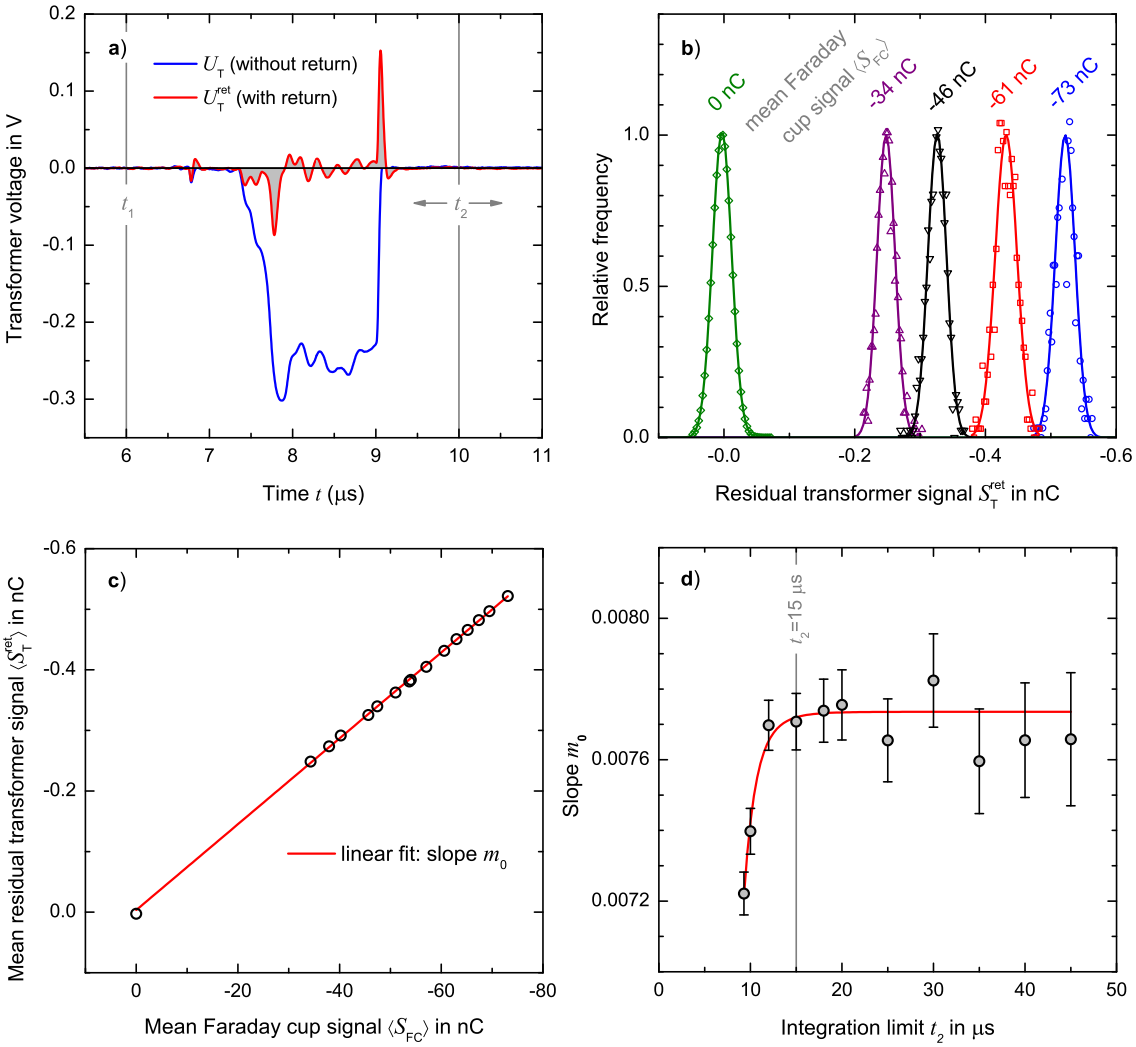


**Figure 16**. a) transformer voltage with return of the charge from the Faraday cup through the transformer via the Q-loop $U_T^{ret}$ as a function of time (red curve) in comparison with the transformer voltage without return $U_T$ (blue curve). Beam pulse charge: about −54 nC. Pulse integration limits: $t_1 = 6$ $\mu$s and $t_2 \geq 9.3$ $\mu$s. b) histogram of residual transformer signals $S_T^{ret}$ at return of the Faraday cup charge through the transformer for five different beam intensities for about 500 beam pulses in each case. The corresponding mean Faraday cup signal $\langle S_{FC} \rangle$ is indicated in each case. Curves: Gaussian fits. c) mean residual transformer signal $\left\langle S_T^{ret} \right\rangle$ at the return of the Faraday cup charge as a function of the mean Faraday cup signal $\langle S_{FC} \rangle$ for different beam intensities. Red line: linear fit with slope $m_0$. d) slope $m_0$ of the linear fit as a function of the integration limit $t_2$. Curve: to guide the eye. Bars: contribution to the expanded uncertainty due to noise.

2017 JINST 12 P03003

Figure 16a shows the residual transformer voltage $U_T^{ret}$ at the return of the Faraday cup current through the ICT via the Q-loop in comparison with a transformer voltage $U_T$ without return. Since the current from the Faraday cup transits the ICT with a certain delay with respect to the beam pulse, the signal is not immediately canceled. Instead, negative or positive spikes appear where the beam pulse shape features falling or rising edges, respectively. However, the residual transformer signal at the return of the Faraday cup current

$$S_T^{ret} = \epsilon \int_{t_1}^{t_2} U_T^{ret}(t)\mathrm{d}t \tag{5.1}$$

is not influenced by the oscillating shape of $U_T^{ret}(t)$. The loss $L$ of the Faraday cup is given by the ratio of the transformer signal "with return" to "without return" $L = (S_T^{ret} - b_0)/(S_T - b_1)$, both corrected with respect to a possibly different offset due to synchronous noise $b_0$ or $b_1$, respectively. However, it is not possible to measure $S_T^{ret}$ and $S_T$ simultaneously. Therefore $S_T^{ret}$ is measured as a function of the Faraday cup signal $S_{FC}$, since the corresponding $S_T(S_{FC})$ is known from the calibration as $S_T = m_1 \cdot S_{FC} + b_1$. $S_{FC}$ and $S_T^{ret}$ are alternately measured[25] by means of a coaxial relay (Tohtsu / Toyo Tsusho CX-230), which switches randomly between feeding the Faraday cup current in the electrometer or in the Q-loop. Figure 16b shows the histograms of the residual transformer signals $S_T^{ret}$ for different beam intensities. The mean residual transformer signal $\left\langle S_T^{ret} \right\rangle$ is determined from the center of the Gaussian fit in each case (curves). The measured corresponding mean Faraday cup signal $\langle S_{FC} \rangle$ is indicated. $\left\langle S_T^{ret} \right\rangle$ is a linear function of $\langle S_{FC} \rangle$ as is obvious from figure 16c. From the slope $m_0$ of the linear fit $\left\langle S_T^{ret} \right\rangle = m_0 \cdot \langle S_{FC} \rangle + b_0$ the Faraday cup collection efficiency $\eta = 1 - L$ can be determined by

$$\eta = 1 - (S_T^{ret} - b_0)/(S_T - b_1) \tag{5.2a}$$
$$= 1 - (m_0 \cdot S_{FC})/(m_1 \cdot S_{FC}) \tag{5.2b}$$
$$= 1 - m_0/m_1 \tag{5.2c}$$
$$= 1 - m_0 \cdot N_T. \tag{5.2d}$$

A reliable determination of $\eta$ has to be independent of the integration limit $t_2$ in eq. (5.1) (see figure 16a). Figure 16d shows the slope $m_0$ as a function of $t_2$. The bars denote the expanded uncertainty of the slope from the linear fit. A signal droop is not resolved in the post-pulse data of $U_T^{ret}$ and thus does not affect $m_0(t_2)$. However, although the beam pulse and the oscillation of $U_T^{ret}$ seem to be over at $t \approx 9.3$ $\mu$s, the $m_0(t_2)$ curve does not converge before $t_2 = 15$ $\mu$s (dashed line) to its asymptotic value of $m_0 \approx 0.0077$. The delayed part of the signal with $t > 9.3$ $\mu$s is supposed to be caused by reflections and transit time effects. Thus it belongs to the complete residual transformer signal. Therefore only data points with $t_2 > 15$ $\mu$s (vertical line) are considered for the determination of $\eta$.

The gray diamonds in figure 17 show the results of eq. (5.2d) as a function of $t_2$. The droop effect which results in an increase of $N_T$ with $t_2$ (see figure 15) affects the results only marginally.

[25] The simultaneous measurement of $S_T^{ret}$ and $S_{FC}$ with the electrometer at the output of the Q-loop changes the shape of the Faraday cup current and thus the shape of $U_T^{ret}(t)$ due to signal reflections.



2017 JINST 12 P03003

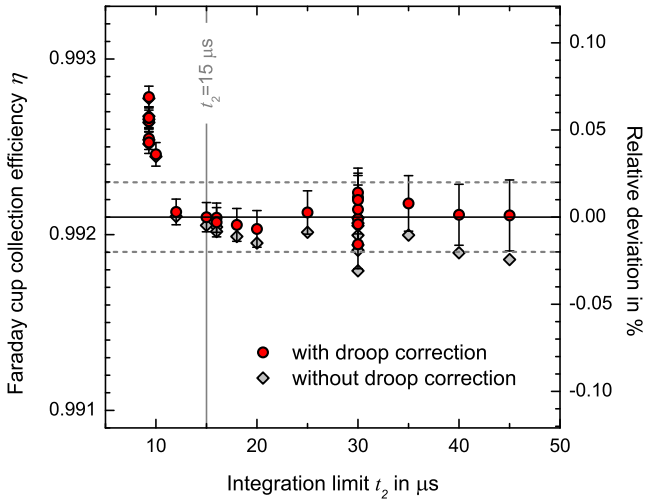


**Figure 17**. Faraday cup collection efficiency $\eta$ (at 27 MeV) determined by eq. (5.2d) as a function of the integration limit $t_2$. Red circles: with correction with respect to the signal droop. Bars: contribution to the expanded uncertainty due to noise. Gray diamonds: without droop correction.

This becomes obvious by the comparison to the results using a calibration factor corrected with respect to the droop contribution determined from post-pulse data (red circles). The uncertainty due to the droop effect is estimated to be $u_{\mathrm{de}}(\eta)/\eta = 0.01$ %. Since $m_0(t_2)$ does not converge before $t_2 = 15$ $\mu$s, the $\eta(t_2)$ curve does not converge before $t_2 = 15$ $\mu$s as well. The Faraday cup collection efficiency $\eta$ (for 27 MeV electrons) determined from the mean value for $t_2 > 15$ $\mu$s (vertical line) is $\eta = 0.9921$. The maximum deviations are within ±0.02 % (dashed lines). The standard deviation is 0.0076 %. The resulting expanded statistical uncertainty contribution is $u_{\mathrm{stat}}(\eta)/\eta = 0.001$ %.

Neither the Faraday cup nor the Q-loop are designed to match the 50 Ω termination and the impedance of the RG58 cable which connects both during the cancellation measurement. Thus $U_{\mathrm{T}}^{\mathrm{ret}}(t)$ (see figure 16a) may be influenced by spikes due to reflections or other effects caused by impedance mismatches. In order to reveal the presence of such effects and a possible influence on the determination of $\eta$, the shape of the canceling current from the Faraday cup which is fed in the Q-loop is varied by means of a capacitor $C_{\mathrm{FC}}$ at the Faraday cup (see figure 3). The shape of the resulting current peak is dominated by the charging and discharging of the additional capacity. Figure 18a shows as an example the time-resolved Faraday cup current for a typical beam pulse if no capacitor or a capacitor with $C_{\mathrm{FC}} = 5.6$ nF or 16.8 nF is installed at its output. The red curve in figure 18b shows the residual transformer voltage curve $U_{\mathrm{T}}^{\mathrm{ret}}(t)$ with $C_{\mathrm{FC}} = 5.6$ nF. At the beginning of the pulse $U_{\mathrm{T}}^{\mathrm{ret}}$ is negative due to the incomplete cancellation of the induction of the beam, since a part of the counteracting Faraday cup current is absorbed by the capacitor. After the beam pulse is finished at $t \approx 9.3$ $\mu$s, the voltage becomes positive with an exponential decay induced by the decreasing current from the discharging capacitor. This behavior is more pronounced with larger capacities as illustrated by the blue curve for $C_{\mathrm{FC}} = 16.8$ nF. The area under the latter curve (blue stripes) is about 10 times larger than the area under the black curve from measurement without an additional capacitor. However, the residual transformer signal $S_{\mathrm{T}}^{\mathrm{ret}}$ is independent of the shape of the $U_{\mathrm{T}}^{\mathrm{ret}}(t)$ curve if the integration limit is set sufficiently large ($t_2 = 30$ $\mu$s) in order to capture



2017 JINST 12 P03003

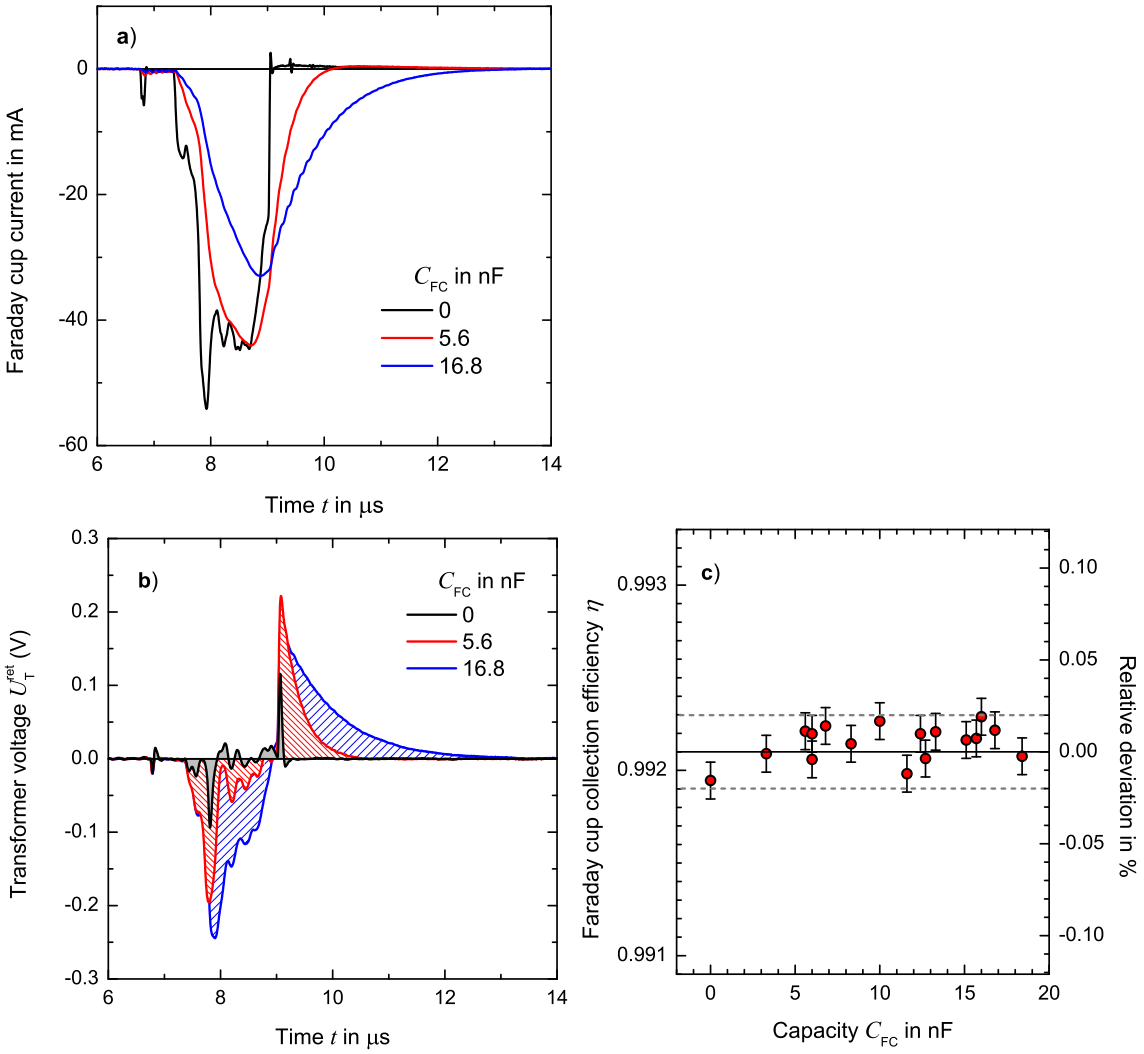


**Figure 18**. a) current of a typical beam pulse from the Faraday cup as a function of time if no capacitor (black) or a capacitor with $C_{FC}$ = 5.6 nF (red) or 16.8 nF (blue) is installed at the Faraday cup output. b) transformer voltage $U_T^{ret}$ at return of the current from the Faraday cup through the ICT via the Q-loop wire as a function of time for different additional capacitors $C_{FC}$ as indicated. Beam pulse charge: about −70 nC. c) faraday cup collection efficiency $\eta$ (at 27 MeV) as a function of the additional capacity $C_{FC}$ ($t_2$ = 30 $\mu$s). Right y-axis: deviation from mean value. Dashed lines: limits for ±0.02 % deviation. Bars: contribution to the expanded uncertainty due to noise.

the complete positive tail. Figure 18c shows the Faraday cup collection efficiency $\eta$ as determined from eq. (5.2d) as a function of $C_{FC}$, i.e. as a function of the shape of the $U_T^{ret}(t)$ curve. The results agree within ±0.02 % deviation from the mean value (dashed lines). Since $\eta$ is independent of the shape of $U_T^{ret}(t)$, significant effects due to spikes or bandpass effects can be excluded.

## 5.2 Beam alignment

Figure 19a shows the horizontal and vertical beam profiles, i.e. the normalized integrated beam intensity as a function of the position with respect to the center of the beamline, of the aligned beam



2017 JINST 12 P03003

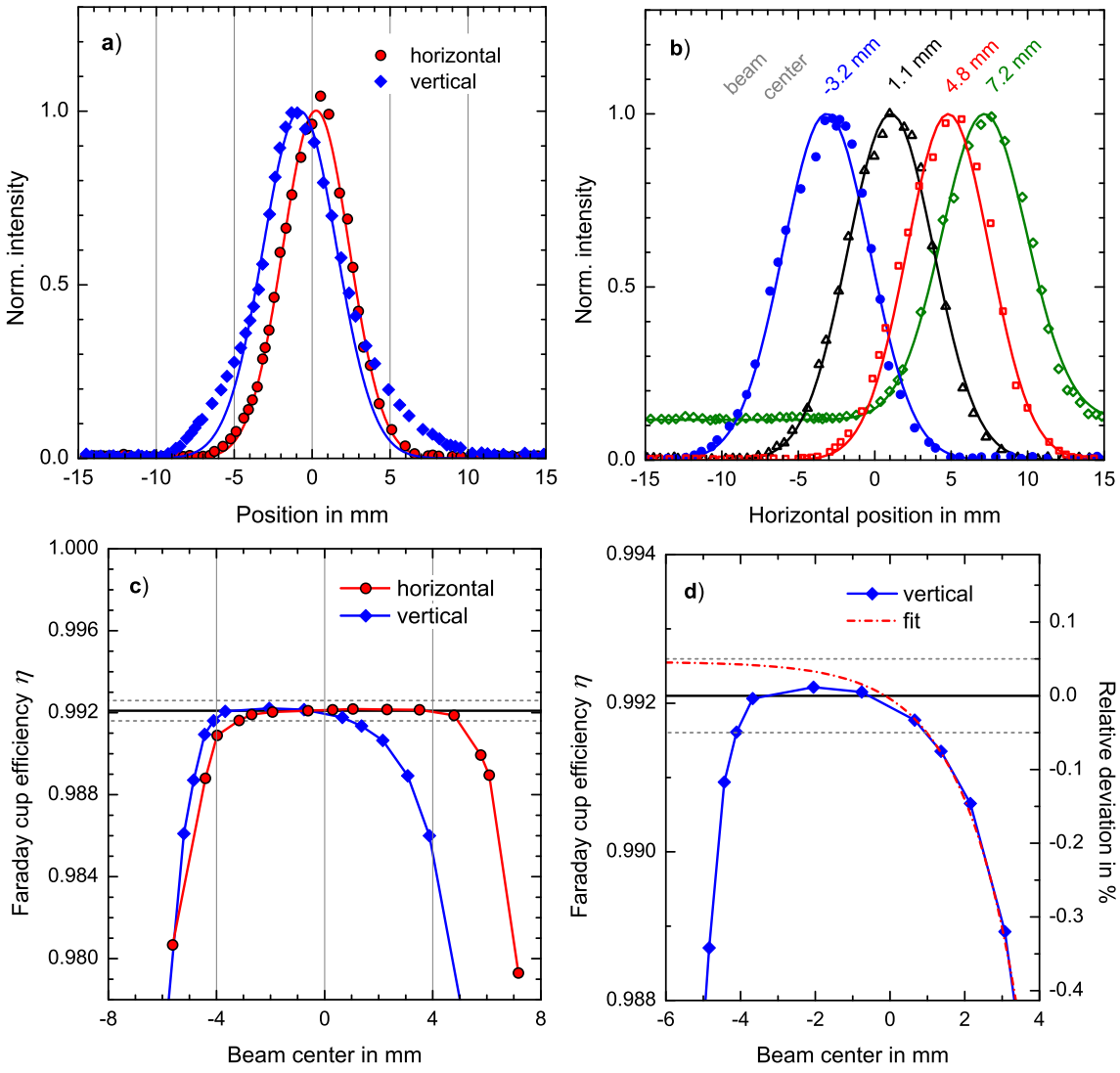


**Figure 19**. a) normalized beam intensity of the aligned beam as used for the determination of the collection efficiency $\eta$ as a function of the horizontal (red circles) and the vertical (blue diamonds) position, respectively, with respect to the center of the beamline as recorded by means of the beam profile monitor (wire scanner) between the current transformer and the Faraday cup. Curves: Gaussian fits. b) normalized beam intensity of the beam as a function of the horizontal position for four different horizontal deflections of the beam. Curves: Gaussian fits (center values are indicated). c) Faraday cup collection efficiency $\eta$ (at 27 MeV) determined by eq. (5.2d) as a function of the beam center of the deflected beam. Red circles: horizontal deflection. Blue diamonds: vertical deflection. Dashed lines: limits for ±0.05 % deviation. d) same data as shown in figure 19c for vertical deflection on enlarged scale. Right y-axis: deviation from maximum value. Dashed lines: limits for ±0.05 % deviation. Red dash-dotted line: fit for data with beam center > −1 mm and extrapolation for < −1 mm.

2017 JINST 12 P03003

as used for the measurements.[26] The beam profiles are recorded by means of a beam profile monitor installed between the current transformer and the Faraday cup. The divergence of the beam was found to be negligibly small ($< 0.1°$) from the comparison of the beam profiles recorded with two further beam profile monitors installed along the beamline. In order to check effects from the lateral tails of the beam on the determination of the Faraday cup collection efficiency, the position of the beam is varied with respect to the center of the beamline and, thus, with respect to the center of the Faraday cup. By adjusting the current of a steerer magnet about 1 m upstream of the ICT, the beam is deflected ($< 0.5°$) and thereby approximately shifted parallel within the beamline between the ICT and the Faraday cup. The symbols in figure 19b represent the measured horizontal beam profiles, for four different horizontal deflections of the beam. They correspond to normal distributions as is obvious by the fitted Gaussian functions (curves). The position of the center of the Gaussian is indicated in each case. For large shifts, as, e.g., for 7.2 mm (green curve), small fractions from the tail of the beam hit the walls of the beamline (35 mm inner diameter) and induce an approximately isotropic background of secondary electrons observable as an offset to the Gaussian distribution. Such secondary electrons may influence the determination of the collection efficiency of the Faraday cup even if their fraction is small and not detectable by the beam profile monitor.

Figure 19c shows the Faraday cup collection efficiency $\eta$ as determined via eq. (5.2) as a function of the position of the beam center at horizontal and vertical deflection, respectively. The beam can be horizontally shifted from $-2$ mm to $+4$ mm without any impact on the determined $\eta$ (agreement within $\pm 0.01$ %). Thus in this range the complete beam is caught by the Faraday cup and effects from projectiles from the tails are not detectable. For beams which have a horizontal shift of $< -3$ mm or $> +5$ mm the deviation from the maximum at the plateau region exceeds $-0.05$ % (lower dashed line). In vertical direction the beam can be shifted only up to $+1$ mm before deviations from the maximum value exceed $-0.05$ %. The asymmetry is caused by an asymmetry of the vertical beam profile (blue curve in figure 19a), where the tail to positive vertical positions is more pronounced than at a Gaussian distribution.[27] Figure 19d shows the same data as shown in figure 19c for the vertical deflected beam on an enlarged scale. The plateau region is not well-defined in this case. For a beam center $> -2$ mm the determination of $\eta$ is influenced by the pronounced beam tail with positive vertical positions, but for a beam center $< -2$ mm the beam tail with negative vertical positions may already influence the result. The red dash-dotted line is an assumption for a reasonable extrapolation without influences from the beam tail with negative vertical positions from a fit on the data with beam center $> -1$ mm. From the asymptotic value the uncertainty of the maximum of $\eta$ due to effects from the vertical tails of the beam is estimated to be $u_{\mathrm{vt}}(\eta)/\eta = 0.05$ % (dashed lines).

All measurements are carried out with a sufficiently aligned beam,[28] i.e. where the beam center is within the plateau region of the dependence of $\eta$ on the beam position. The relative expanded uncertainty contribution due to effects from tails of the beam on the determined Faraday cup efficiency is estimated to be $u_{\mathrm{t}}(\eta)/\eta = 0.05$ %.

[26] Note: the used wire scanner integrates the beam intensity along the wire. Thus the horizontal or vertical beam profiles are the integrated intensity perpendicular to the horizontal or vertical direction, respectively.

[27] Attempts to modify the beam profile by means of an additional collimator close in front of the ICT do not succeed because of the collateral production of secondary electrons.

[28] The beam center is aligned by means of steerer magnets to $0 \pm 1$ mm horizontal position and $-1 \pm 1$ mm vertical position with respect to the center of the beamline.



2017 JINST 12 P03003

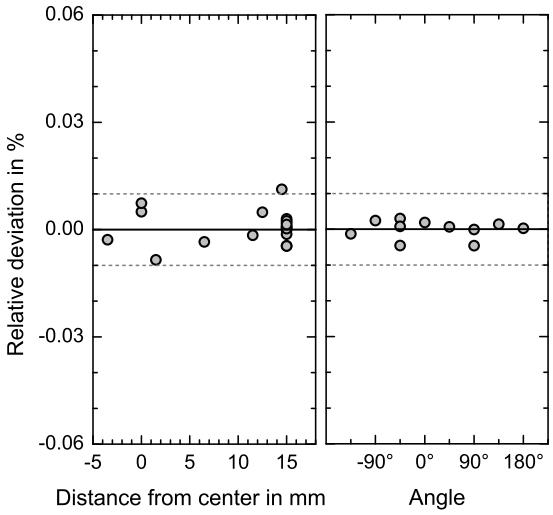


**Figure 20**. Deviations from the average transformer signal as a function of the distance of the axis of the Q-loop wire from the center of the ICT aperture of 17 mm radius (left) and as a function of the angle of rotation of the Q-loop at the inner edge of the ICT aperture with respect to the connector (right).

For an ideal coil the position where the beam or the Q-loop wire passes through a current transformer is irrelevant. For real Rogowski coils, inhomogeneities at the spacing in the coil winding, in particular at the ends of the winding, may give rise to variations in the induction by the magnetic field resulting in a position dependence on the rim of the coil. For certain models of the Bergoz ICT at the inner edge of the ICT aperture, deviations of up to 2 % are reported [33]. Since the Q-loop wire is placed at the inner edge of the ICT aperture (see right side of figure 2b), the spatial homogeneity of the used ICT is investigated. The Q-loop is shifted to the center of the ICT aperture and along the inner edge by rotating the ICT between the additional flanges with the electrical feedthroughs, while a charge pulse of nominal −60 nC with 2 $\mu$s length from the charge pulse generator is fed into the Q-loop. Figure 20 shows the deviations from the average transformer signal as a function of the distance from the center of the ICT aperture and as a function of the angle of rotation, respectively. The deviations scatter within ±0.01 % (dashed lines). Hence the expanded uncertainty contribution due to the spatial inhomogeneity of the ICT, i.e. due to the different position of the beam and the Q-loop, is estimated to be $u_{\mathrm{ih}}(\eta)/\eta = 0.01$ %.

**Table 4**. Contributions to the expanded relative uncertainty ($k = 2$) of the collection efficiency $\eta$ determined by the cancellation measurement. The last column refers to the corresponding figures of the data on which the uncertainty estimation is based.

| | Uncertainty contribution | Type | Uncertainty in % | Figure |
|---|---|---|---|---|
| $u_{\mathrm{de}}(\eta)$ | due to the droop effect | B | 0.01 | 17 |
| $u_{\mathrm{stat}}(\eta)$ | statistical contribution | A | 0.001 | 17 |
| $u_{\mathrm{t}}(\eta)$ | due to tails of the beam | B | 0.05 | 19c |
| $u_{\mathrm{ih}}(\eta)$ | spatial inhomogeneity of the ICT | B | 0.01 | 20 |
| $u_{\mathrm{c}}(\eta)$ | combined | | 0.052 | |



2017 JINST 12 P03003

In conclusion, the collection efficiency of the Faraday cup for 27 MeV electrons is determined by a cancellation measurement to $\eta = 0.9921$. The combined expanded relative uncertainty amounts to $u_c(\eta)/\eta = 0.052$ %. Table 4 summarizes the uncertainty contributions.

### 5.3 Simulation

The experimentally determined collection efficiency is compared with the results of a MC simulation carried out by means of EGSnrc [22, 23]. The simulations consist of a parallel beam 2 mm in diameter which impinges perpendicularly on the center of the Faraday cup model as shown on the right side of figure 4, including the vacuum flange (steel) behind the back of the Faraday cup. At two planes, one at the entrance of the Faraday cup and one between the rear and the vacuum flange, forward and backscattered electrons and positrons are counted for a charge balance. The number of electrons which impinge on the entrance is $n_{\text{in}}^{\text{entr}}(e^-) = 10^6$. Charge losses are the number of backscattered electrons at the entrance $n_{\text{out}}^{\text{entr}}(e^-)$, photon-induced electrons which escape in rear direction $n_{\text{out}}^{\text{rear}}(e^-)$ and positrons backscattered from the vacuum flange to the Faraday cup $n_{\text{in}}^{\text{rear}}(e^+)$. On the other hand, there is a gain from positrons which escape at the rear $n_{\text{out}}^{\text{rear}}(e^+)$, electrons backscattered from the vacuum flange $n_{\text{in}}^{\text{rear}}(e^-)$ and backscattered positrons at the entrance $n_{\text{out}}^{\text{entr}}(e^+)$. The total loss is given by

$$L = \frac{n_{\text{out}}^{\text{entr}}(e^-) + n_{\text{out}}^{\text{rear}}(e^-) + n_{\text{in}}^{\text{rear}}(e^+) - n_{\text{out}}^{\text{rear}}(e^+) - n_{\text{in}}^{\text{rear}}(e^-) - n_{\text{out}}^{\text{entr}}(e^+)}{n_{\text{in}}^{\text{entr}}(e^-)}. \tag{5.3}$$

Electrons with kinetic energies $< 10$ keV are not taken into account in the simulation. They can escape the Faraday cup only if they are produced at most 1 $\mu$m beneath the surface and thus contribute only marginally to the overall loss.

The open circles in figure 21 represent the calculated Faraday cup collection efficiency $\eta = 1 - L$ from eq. (5.3) as a function of the kinetic energy of the beam electrons. The red square indicates the experimental result for 27 MeV from the cancellation measurement described above in subsection 5.1. The difference of 0.25 % between the experiment and the MC simulation is within the usual assumptions and experiences about the accuracy of MC simulations of high energy beams as used in radiotherapy [5, 34]. The MC simulations are based on data sets with associated uncertainties $\geq 1$ % [34, 35] as, e.g., cross section data for the photoelectric effect (2 %), for Compton scattering (1 %), and for pair production (2 %) as well as electron stopping powers based on empirical mean ionization energies (1 % to 10 %) [36]. Thus deviations in the range of some 0.1 % are plausible and the MC result is therefore interpreted as consistent with the value from the cancellation measurement. Estimations of the resulting (nonstatistical) uncertainty contributions in MC calculations are very elaborate (see, for e.g., ref. [34]) and are not carried out here. Thus only the more accurate experimentally determined value (see table 4) is taken into account in the uncertainty budget of the charge measurement.

The gray triangles in figure 21 complement the experimental data by four further energies from preliminary experiments done two years ago, where the ICT has not yet been isolated from the beamline grounding. The collection efficiency is determination by cancellation measurement utilizing a battery operated 8-bit hand-held oscilloscope. Since this oscilloscope is potential-free, noise voltage between local and beamline grounding is avoided. The experimental data points follow the trend of the calculated collection efficiency. However, the deviations increase with



2017 JINST 12 P03003

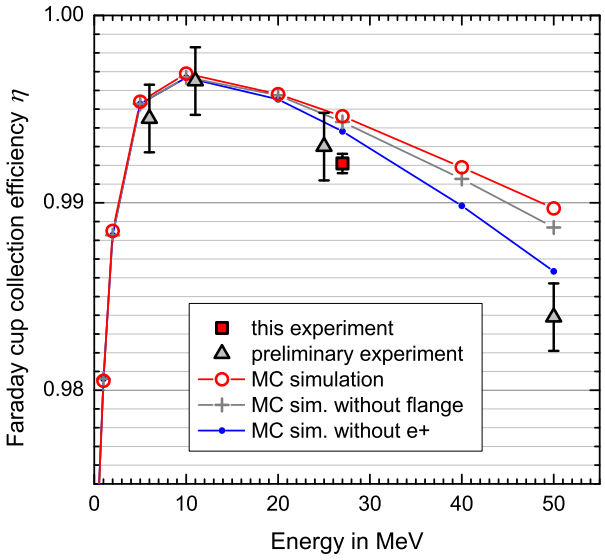


**Figure 21**. Faraday cup collection efficiency $\eta$ as a function of the energy of the electron beam. Red open circles: MC simulation by means of EGSnrc. Red square: result from cancellation measurement for 27 MeV. Gray triangles: results from preliminary experiments utilizing an 8-bit hand-held oscilloscope. Crosses: MC simulation without taking into account the vacuum flange behind the rear of the Faraday cup. Blue dots: MC simulation without taking into account positrons and the vacuum flange.

increasing energy, possibly due to an increasing yield of neutrons combined with activation which is not treated in the EGSnrc code. The exclusion of the vacuum flange behind the rear of the Faraday cup, by neglecting $n_{\text{in}}^{\text{rear}}(e^+)$ and $n_{\text{in}}^{\text{rear}}(e^-)$ in eq. (5.3), affects the results only marginally (gray crosses). Thus a more complex geometry does not change the results. Positrons do not contribute significantly at 27 MeV as is obvious from the results with the additional exclusion of all $n(e^+)$ terms in eq. (5.3) (blue dots).[29]

## 6 Results

The charge of a single beam pulse measured nondestructively by means of the beam intensity monitoring system consisting of current transformer, preamplifier, and waveform digitizer is given by

$$\begin{aligned} Q_{\text{P}} &= S_{\text{FC}}/\eta \\ &= \hat{S}_{\text{T}}/\eta \\ &= N_{\text{T}} \cdot (S_{\text{T}} - b_1)/\eta. \end{aligned} \tag{6.1}$$

The calibration factor $N_{\text{T}}$ is valid for the actual setup (in particular incl. the transmission cable between the ICT and the waveform digitizer) and the chosen integration interval ($t_2$ in eq. (4.1)), i.e. $N_{\text{T}}$ is not a characteristic value of the ICT device. The offset due to synchronous noise $b_1$ is small and can be neglected in many cases (in particular at $t_2 = 9.3\ \mu$s). The collection efficiency of the Faraday cup for 27 MeV electrons is determined experimentally to be $\eta = 0.992$,

[29]The number of backscattered positrons is negligible $\left(\frac{n_{\text{out}}^{\text{entr}}(e^+)}{n_{\text{in}}^{\text{entr}}(e^-)} < 0.02\ \%, \frac{n_{\text{in}}^{\text{rear}}(e^+)}{n_{\text{in}}^{\text{entr}}(e^-)} < 0.02\ \%\right)$.



2017 JINST 12 P03003

**Table 5**. Contributions to the expanded relative uncertainty ($k = 2$) for the nondestructive measurement of the charge $Q_P$ of a single beam pulse of about −60 nC of a 27 MeV linac beam by means of the beam intensity monitoring system. The last column refers to the corresponding table of the considered uncertainty contributions.

| | Uncertainty contribution | Type | Uncertainty in % | Table |
|---|---|---|---|---|
| $u_c(\hat{S}_T)$ | transformer signal calibration[a] | B | 0.063 | 3 |
| $u_c(\eta)$ | collection efficiency determination | B | 0.052 | 4 |
| $u_c(Q_P)$ | combined | | 0.082 | |

[a] For $t_2 = 9.3\ \mu s$.

which is described consistently by MC simulations. The expanded relative uncertainty of the nondestructive measurement of a single 27 MeV linac beam pulse of about −60 nC amounts to $u_c(Q_P)/Q_P = 0.082$ %. Table 5 summarizes the uncertainty contributions.

## 7 Summary

The nondestructive absolute measurement of the charge $Q_P$ of single beam pulses of about −60 nC of a 27 MeV electron beam from an electron linear accelerator is demonstrated. The performance of the applied beam intensity monitoring system consisting mainly of a Bergoz ICT, a preamplifier, a coaxial cable, and a waveform digitizer is analyzed. The signal acquisition is optimized in order to eliminate significant effects from synchronous noise, induced by interferences emitted from the running linac. The precision and the linearity of the system are studied which reveal a sufficiently small statistical uncertainty contribution for pulse-resolved measurements and that a systematic linearity error is not observable. The signal of the beam intensity monitoring system $S_T$ is calibrated against a custom-made Faraday cup which shares the same vacuum as the linac beam. The design of the Faraday cup is optimized with regard to high collection efficiency for electron beams with energies of 6 MeV to 50 MeV at small overall size. The collection efficiency for 27 MeV is determined to 99.2 % by a cancellation measurement where the beam current, measured by means of the ICT, is compared with the current from the Faraday cup measured by the same ICT. For this purpose, the Faraday cup current is fed back through the ICT by means of a wire additionally mounted in situ inside the ICT aperture. The experimentally determined collection efficiency is consistent with the result from a MC simulation. The measurement of the charge collected by the Faraday cup is carried out by an analog electrometer in combination with a high-accuracy digital multimeter. The electrometer is calibrated in situ by a reference charge traceable to primary standards. In order to check the applicability of the electrometer to pulsed charges, the measurement of constant charge pulses from a charge pulse generator is compared with two further independent methods and, thereby, traced back to different measurands and primary standards. Since the results of three methods agree, significant errors due to the pulsed character of the charge to be measured are implausible. By the calibration of the signal of the beam intensity monitoring system against the simultaneously measured corresponding charge from the Faraday cup, deficiencies, as, e.g., due to the voltage loss at the coaxial cable or due to the transformer signal droop, are fully included in the calibration factor.



2017 JINST 12 P03003

In conclusion, the charge of each individual beam pulse at the high-energy beamline of the research electron linac of the PTB can be measured nondestructively in real time, traceable to primary standards with a relative expanded measurement uncertainty $< 0.1$ %.

## References


[1] K. Derikum, *A dedicated irradiation facility for radiotherapy dosimetry*, *World Congress on Medical Physics and Biomedical Engineering* **25/1** (2009) 53.

[2] K.B. Unser, *Design and preliminary tests of a beam intensity monitor for LEP*, in proceedings of the *1989 Particle Accelerator Conference*, Chicago, U.S.A., March 20–23, 1989.

[3] J. Bergoz, *Current monitors for particle beams*, *Nucl. Phys.* **A 525** (1991) 595.

[4] Bergoz Instrumentation, Saint-Genis-Pouilly, France, www.bergoz.com.

[5] F. Renner, J. Wulff, R.-P. Kapsch and K. Zink, *Uncertainties in Monte Carlo-based absorbed dose calculations for an experimental benchmark*, *Phys. Med. Biol.* **60** (2015) 7637.

[6] F. Renner, *Benchmark-Experiment zur Verifikation von Strahlungstransportrechnungen für die Dosimetrie in der Strahlentherapie*, *Z. Med. Phys.* **26** (2016) 209.

[7] F. Renner, A. Schwab, R.P. Kapsch, C. Makowski and D. Jannek, *An approach to an accurate determination of the energy spectrum of high-energy electron beams using magnetic spectrometry*, 2014 *JINST* **9** P03004.

[8] GUM, *Evaluation of measurement data – Guide to the expression of uncertainty in measurement*, *JCGM* **100** (2008) 1.

[9] B. Hidding et al., *Novel method for characterizing relativistic electron beams in a harsh laser-plasma environment*, *Rev. Sci. Instrum.* **78** (2007) 083301.

[10] M.E. Conde, W. Gai, R. Konecny, X. Li, J. Power, P. Schoessow and N. Barov, *Generation and acceleration of high-charge short-electron bunches*, *Phys. Rev. ST Accel. Beams* **1** (1998) 041302.

[11] M. Alves et al., *PHIL photoinjector test line*, 2013 *JINST* **8** T01001.

[12] Y. C. Wu, B. Zhu, K.G. Dong, Y.H. Yan and Y.Q. Gu, *Note: Absolute calibration of two DRZ phosphor screens using ultrashort electron bunch*, *Rev. Sci. Instrum.* **83** (2012) 026101.

[13] K. Zeil et al., *Absolute response of fuji imaging plate detectors to picosecond-electron bunches*, *Rev. Sci. Instrum.* **81** (2010) 013307.

[14] K. Nakamura et al., *Electron beam charge diagnostics for laser plasma accelerators*, *Phys. Rev. ST Accel. Beams* **14** (2011) 062801.

[15] K. Wittenburg, *Specific instrumentation and diagnostics for high-intensity hadron beams*, in *CERN Accelerator School: High Power Hadron Machines*, Bilbao, Spain, 24 May–2 Jun 2011, CERN-2013-001.251 [arXiv:1303.6767].

[16] J. Pruitt, *Electron beam current monitoring system*, *Nucl. Instrum. Meth.* **92** (1971) 285.

[17] P.C. Dunn, *Absolute beam charge measurements with toroid monitors: Experience at the Bates Linac*, *Nucl. Instrum. Meth.* **165** (1979) 163.

[18] D.G. Pellinen, M.S. Di Capua, S.E. Sampayan, H. Gerbracht and M. Wang, *Rogowski coil for measuring fast, high level pulsed currents*, *Rev. Sci. Instrum.* **51** (1980) 1535.




2017 JINST 12 P03003

[19] P. Forck, *Lecture notes on beam instrumentation and diagnostics*, in *Joint University Accelerator School 2011*, Darmstadt, Germany (2011).

[20] J.-C. Denard, *Beam current monitors*, in *CERN Accelerator School on Beam Diagnostics*, Le Normont, Dourdan, France, 28 May–6 June 2008, CERN-2009-005.

[21] H. Koziol, *Beam diagnostics for accelerators*, in *CERN Accelerator School: 5th General Accelerator Physics Course*, Jyväskylä, Finland, Sept. 7–18, 1994.

[22] I. Kawrakow, E. Mainegra-Hing, D. Rogers, F. Tessier and B. Walters, *The EGSnrc code system: Monte Carlo simulation of electron and photon transport*, *NRCC Report* **PIRS-701** (2013) 1.

[23] D. Rogers, B. Walters and I. Kawrakow, *BEAMnrc users manual*, *NRCC Report* **PIRS-0509a** (2015) 1.

[24] K.L. Brown and G.W. Tautfest, *Faraday cup monitors for high energy electron beams*, *Rev. Sci. Instrum.* **27** (1956) 696.

[25] J. Kretschko, D. Harder and W. Pohlit, *Absolutmessung der Teilchenflussdichte schneller Elektronen mit einem Faraday-Käfig*, *Nucl. Instrum. Meth.* **16** (1962) 29.

[26] M. Vognar, C. Simane and D. Chvatil, *Faraday cup for electron flux measurements on the microtron MT 25*, *Acta Polytech.* **41** (2001) 11.

[27] S. Gardiner, J. Matthews and R. Owens, *An accurate non-intercepting beam current integrator for pulsed accelerator beams*, *Nucl. Instrum. Meth.* **87** (1970) 285.

[28] CGC Instruments, Chemnitz, Germany, http://www.cgc-instruments.com.

[29] *Model 439 digital current integrator operating manual*, ORTEC, a subsidiary of AMETEK, Inc.

[30] R.C. Webber, *Fermilab tutorial on beam current monitoring*, *Fermilab* **Conf-00-119** (2000) 83.

[31] R.C. Webber, *Tutorial on beam current monitoring*, *AIP Conf. Proc.* **546** (2016) 83.

[32] J. Hinkson, *Advanced Light Source*, unpublished.

[33] J. Bergoz, *Integrating Current Transformer (ICT) pulse charge accuracy*, Technical Note ICT / 06.1, (2006).

[34] J. Wulff, J.T. Heverhagen, K. Zink and I. Kawrakow, *Investigation of systematic uncertainties in Monte Carlo-calculated beam quality correction factors*, *Phys. Med. Biol.* **55** (2010) 4481.

[35] J.H. Hubbell, *Review and history of photon cross section calculations*, *Phys. Med. Biol.* **51** (2006) R245.

[36] ICRU, *Stopping Powers for Electrons and Positrons*, ICRU report 37 (1984).

2017 JINST 12 P03003